

C. SCHULZ<sup>1,✉</sup>  
B.F. KOCK<sup>1</sup>  
M. HOFMANN<sup>1</sup>  
H. MICHELSEN<sup>2</sup>  
S. WILL<sup>3</sup>  
B. BOUGIE<sup>4</sup>  
R. SUNTZ<sup>5</sup>  
G. SMALLWOOD<sup>6</sup>

## Laser-induced incandescence: recent trends and current questions

<sup>1</sup> IVG, Universität Duisburg-Essen, Duisburg, Germany

<sup>2</sup> Combustion Research Facility, Sandia National Laboratories, Livermore, CA, USA

<sup>3</sup> Technische Thermodynamik, Universität Bremen, Bremen, Germany

<sup>4</sup> Applied Molecular Physics, Institute for Molecules and Materials, Radboud University Nijmegen, The Netherlands

<sup>5</sup> Institut für Technische Chemie und Polymerchemie, Universität Karlsruhe, Karlsruhe, Germany

<sup>6</sup> National Research Council Canada, Ottawa, Canada

Received: 28 February 2006/Revised version: 16 April 2006

Published online: 9 May 2006 • © Springer-Verlag 2006

**ABSTRACT** This paper provides an overview of a workshop focused on fundamental experimental and theoretical aspects of soot measurements by laser-induced incandescence (LII). This workshop was held in Duisburg, Germany in September 2005. The goal of the workshop was to review the current understanding of the technique and identify gaps in this understanding associated with experimental implementation, model descriptions, and signal interpretation. The results of this workshop suggest that uncertainties in the understanding of this technique are sufficient to lead to large variability among model predictions from different LII models, among measurements using different experimental approaches, and between modeled and measured signals, even under well-defined conditions. This article summarizes the content and conclusions of the workshop, discusses controversial topics and areas of disagreement identified during the workshop, and highlights recent important references related to these topics. It clearly demonstrates that despite the widespread application of LII for soot-concentration and particle-size measurements there is still a significant lack in fundamental understanding for many of the underlying physical processes.

PACS 44.05.+e; 47.70.Pq; 78.70.-g; 65.80.+n; 78.20.Ci

### 1 Introduction

Laser-induced incandescence (LII) has proven to be a powerful tool for particle-concentration and primary particle-size measurements in combustion, particle synthesis, and environmental applications. LII has been particularly useful for applications to practical combustion systems for which various experimental approaches and data evaluation techniques have been developed. Several research groups are working on improving the fundamental understanding of LII with the aim of turning LII into a truly quantitative diagnostic, but interactions between these groups have been limited. In order to enhance communication between researchers in this area, a workshop was held in September 2005 in Duisburg, Germany. The primary goal of the workshop was to define the status quo on LII and to determine gaps in the understanding of LII related to experimental issues, modeling,

and signal interpretation. The papers presented in this special feature result from contributions to this workshop. During this two-day workshop, the most ‘burning’ issues in LII science were discussed.

This article gives an overview of the content and conclusions of the workshop, highlights recent important publications on LII, and presents controversial topics and areas of disagreement identified in the comparison of different models and measurement approaches. Despite extensive application of LII to many practical diagnostics problems and development of commercial instruments for routine implementation of LII, these comparisons demonstrate significant shortcomings in the fundamental understanding of LII and, hence, in the interpretation of measurement results.

LII involves heating particles with a laser and measuring the resulting radiative emission. The magnitude of the LII signal is correlated with the volume fraction of particles in the detection region, and the decay rate of the LII signal is mainly governed by the specific surface of the particles, which in turn depends on primary particle size. LII has been used extensively for qualitative measurements of soot temporal and spatial distributions [1–6]. Several groups have attempted to extend these applications to quantitative measurements of volume fraction and primary particle size [6–25]. Such measurements require a firm understanding of the factors that influence LII signals.

Many attempts have been made to model the processes involved in generating the LII signal [4, 11, 12, 17, 21, 23, 26–44]. These models generally account for particle heating by laser absorption and cooling by conduction to the surrounding atmosphere, sublimation of carbon clusters, and radiative emission. They also account for size changes resulting from sublimation. They have been used to test the sensitivity of LII to factors such as primary particle and aggregate size distributions and particle phase changes. Such models are useful for data interpretation and for identifying areas of greatest uncertainty in the understanding of LII.

The results of this workshop indicate that the current understanding of LII is limited enough to lead to wide variability in LII model predictions and experimental results, even under well-defined conditions. Further advances in this field will be required to narrow the uncertainties in these measurements to acceptable levels. The next three sections of this paper present the status of LII, identify the open questions, and recommend

✉ Fax: +49-203-379-3087, E-mail: christof.schulz@uni-due.de

targets for further research in the following areas: modeling of the LII signal (Sect. 2), experimental issues of LII measurements (Sect. 3), and evaluation of experimentally obtained LII data (Sect. 4). The final section (Sect. 5) presents a comparison of results from the analysis of one experimental data set evaluated by several groups using their respective data analysis approaches. A comparison is also presented for measurements carried out on pre-defined target flames in different laboratories.

The collaboration between groups initiated at this LII workshop will be continued in order to solve the remaining problems. Future meetings will be held in the form of a bi-annual workshop series, starting with the next workshop which will take place in August 2006.

## 2 Modeling of LII signal

### 2.1 Motivation

A number of models have been developed to describe the heating and cooling mechanisms important for LII detection of soot [4, 11, 12, 17, 21, 23, 26–42, 44]. These models are frequently used to analyze LII data, particularly time-resolved signals recorded for primary particle sizing [11, 12, 17, 23, 30, 32, 35–38, 42]. The models are also used to investigate the physics and chemistry involved in laser heating of soot particles to temperatures at which they incandesce ( $> \sim 2500$  K) [17, 21, 31, 33, 34, 39–41]. Once validated, these models can be used to understand the applicability of LII under a wide range of conditions.

In general these models solve the energy- and mass-balance equations for particle temperature and size. They usually account for particle heating by laser absorption and cooling by radiation, sublimation, and conduction to the surrounding atmosphere. They may incorporate other mechanisms or descriptions of particle characteristics that influence heating or cooling rates, particle-size changes, and LII signals. Particle characteristics of interest include primary particle-size distributions [11, 30, 37, 38, 42, 45], aggregate-size distributions [46] and morphology, and particle composition. Additional mechanisms that may be important in controlling LII signal evolution include primary particle phase changes [39, 40], non-thermal photodesorption of carbon clusters [39, 40], oxidation [39, 40], and thermionic emission [31].

In the modeling sessions of the LII workshop 2005 we performed comparisons of the predicted LII signal from nine models. We focused on identifying the most significant differences between models in common use for analysis of LII data. We also sought to determine aspects of the physical description of LII that lead to the largest uncertainties in signal prediction and analysis. As a final goal, we compiled a list of future directions for model development and a corresponding list of needs for experimental support.

### 2.2 Model input

In order to simplify the interpretation of the model comparison, each model was run with the same input. The models used the same smooth laser temporal profile with a full width at half maximum of 6.9 ns. The laser spatial profile was assumed to be uniform, i.e. each calculation was performed

for a single laser fluence. Signal detection was assumed to be over 610–650 nm with a square band-pass filter and infinitely fast detector. The primary particle size was assumed to be 30 nm and mono-disperse. We performed comparisons for twelve model cases including two excitation wavelengths, two fluences, two temperatures, and two pressures. The cases are described in Table 1. For several of the models the fluence dependence of the peak of the calculated LII temporal profiles was also calculated for 532- and 1064-nm excitation at 1800 K and 1 bar.

### 2.3 Model description

The nine models included in this comparison all solve the energy- and mass-balance equations for temperature and primary particle size. They all account for the rate of change of the sensible energy stored by the particle, which balances the rate of energy increase predominantly by laser absorption and energy dissipation predominantly by conduction, sublimation, and radiation. The signal is calculated either by integrating the Planck function over wavelength or by calculating the intensity at a specific wavelength. For the model comparison presented here, the wavelength region over which the models were integrated was specified, but the band pass was sufficiently narrow that several models calculated the signal only at the central wavelength (Dreier–Bockhorn, Dreier–Roth, Dreier–Schittkowski, Kock–Roth, Liu). A few of the models account for the effects of aggregation on conduction (Kock–Roth, Liu) and on the optical properties (Kock–Roth, Liu, Michelsen) and generally (although not in this study) account for the effects of primary particle-size distributions (Dreier–Bockhorn, Kock–Roth, Liu). One of them includes the effects of photodesorption of carbon clusters, thermionic emission, oxidation, and phase changes (Michelsen). The models are described briefly below, and summaries of how they treat the major terms in the energy- and mass-balance equations are given in Tables 2–4.

*2.3.1 Bladh–Bengtsson.* This model is a modification of the model described by Bladh and Bengtsson [37]. It follows the framework presented by Snelling et al. [33] and Smallwood et al. [34], which is derived from the models presented by Eckbreth [27], Melton [28], and Hofeldt [29]. Absorptive heating, radiative cooling, and signal evolution are calculated using

Case number	Laser wavelength/nm	Ambient pressure/bar	Ambient temperature/K	Laser fluence/J/cm <sup>2</sup>
1	532	1	1800	0.05
2	532	1	1800	0.70
3	532	1	300	0.05
4	532	1	300	0.70
5	532	10	1800	0.05
6	532	10	1800	0.70
7	1064	1	1800	0.05
8	1064	1	1800	0.70
9	1064	1	300	0.05
10	1064	1	300	0.70
11	1064	10	1800	0.05
12	1064	10	1800	0.70

TABLE 1 Description of input conditions used in the model comparison

Model	Internal energy	Absorption	Radiation/signal
Bladh–Bengtsson [37]	$T$ -dependent $\varrho$ , $C_s$	$\lambda$ -dependent $E(m)$ , Rayleigh	Constant $m$ , Rayleigh
Boiarciuc [34]	Constant $\varrho$ , $T$ -dependent $C_s$	$\lambda$ -dependent $E(m)$ , Rayleigh	$\lambda$ -dependent $E(m)$ , Rayleigh
Dreier–Bockhorn [38]	Constant $\varrho$ , $C_s$	Constant $m$ , Rayleigh	Constant $m$ , Rayleigh
Dreier–Roth [30]	Constant $\varrho$ , $T$ -dependent $C_s$	Constant $m$ , Rayleigh	Constant $m$ , Rayleigh
Dreier–Schittkowski [35]	Constant $\varrho$ , $C_s$	Constant $m$ , Rayleigh	Constant $m$ , Rayleigh
Hadef et al. (DLR) [44]	$T$ -dependent $\varrho$ , $C_s$	$\lambda$ -dependent $E(m)$ , Rayleigh	$\lambda$ -dependent $E(m)$ , Rayleigh
Kock–Roth [11, 30, 52, 53]	Constant $\varrho$ , $T$ -dependent $C_s$	Heat-up by two-color pyrometry	Constant $m$ , Rayleigh
Liu (NRC) [33, 34, 46]	Constant $\varrho$ , $T$ -dependent $C_s$	Constant $m$ , RDG	Constant $m$ , RDG
Michelsen (Sandia) [39]	$T$ -, $\varphi$ -dependent $\varrho$ , $C_s$	$\lambda$ -, $\varphi$ -dependent $\sigma_\lambda$ , RDG, 1–3 photons	$\lambda$ -, $\varphi$ -dependent $\varepsilon_\lambda$ , RDG

TABLE 2 Model treatment of particle internal energy, absorptive heating, radiative cooling, and signal prediction

Model	Conduction
Bladh–Bengtsson [37]	Transition regime (McCoy and Cha [48]), $\alpha_T = 0.3$ $T$ -dependent heat capacities, thermal conductivities
Boiarciuc [34]	Transition regime (McCoy and Cha [48]) at low $p$ , $\alpha_T = 0.26$ Continuum regime at high $p$
Dreier–Bockhorn [38]	Free-molecular flow regime, $\alpha_T = 0.2$
Dreier–Roth [30]	Free-molecular flow regime/transition/continuum regimes, $\alpha_T = 1$
Dreier–Schittkowski [35]	Transition regime (McCoy and Cha [48]), $\alpha_T = 0.9$ $T$ -dependent thermal conductivity
Hadef et al. (DLR) [44]	Free-molecular flow regime at low $p$ , $\alpha_T = 0.3$ Transition regime at high $p$
Kock–Roth [11, 30, 52, 53]	Free-molecular flow regime at low $p$ , $\alpha_T < 1$ Transition regime at intermediate $p$ , $\alpha_T < 1$ Continuum regime at high $p$
Liu (NRC) [33, 34, 46]	Transition regime (Fuchs), $\alpha_T = 0.37$
Michelsen (Sandia) [39]	Free-molecular flow regime at low $p$ , $\alpha_T = 0.26$ Transition regime (McCoy and Cha [48]) at high $p$ $T$ -dependent heat capacities, thermal conductivities

TABLE 3 Model treatment of conductive cooling rate

a Rayleigh approximation. Calculations of radiation cooling and signal production are performed with a constant value of 1.56–0.46 i for the index of refraction  $m$  [47]. Absorptive heating uses a wavelength ( $\lambda$ )-dependent value of  $E(m)$ . Conductive cooling rates are calculated using a transition-regime approximation based on the formulation by McCoy and Cha [48] with a thermal accommodation coefficient  $\alpha_T$

of 0.3. Sublimation rates are derived from a temperature ( $T$ )-dependent average mass and enthalpy of formation of sublimed carbon clusters with a mass accommodation coefficient  $\alpha_M$  for all clusters of 0.8. The Clausius–Clapeyron equation and carbon vapor-pressure data from Leider et al. [49] were used to generate a polynomial expression for the average mass of clusters  $C_{ave}$  leaving the surface [34]. Sublimation is calculated for free-molecular flow conditions at all ambient pressures and is assumed to be kinetically controlled, i.e. surface partial pressures of carbon clusters are not influenced by transport rates. In the modified version of the model, temperature-dependent values for heat capacities and thermal conductivity [39] are used to calculate conductive cooling rates, and temperature-dependent density ( $\varrho$ ) and specific heat ( $C_s$ ) are used to calculate the particle internal energy.

**2.3.2 Boiarciuc.** This model reproduces the model described by Smallwood et al. [34] at atmospheric pressure (see the original Bladh–Bengtsson model description above). The thermal accommodation coefficient is 0.26, and the mass accommodation coefficient is 0.8. Absorptive heating, radiative cooling, and signal magnitude are calculated using a Rayleigh approximation. The refractive-index function (derived from  $m$ ) is wavelength dependent (i.e.  $E(m) = 0.232 + \lambda \times 1254.6$  for  $\lambda$  in cm) and is taken from data and analyses presented by Krishnan et al. [50] and fitted by Snelling et al. [41]. At high pressures this model is the same as the Kock–Roth model (see below).

Model	Sublimation
Bladh–Bengtsson [37]	Kinetically controlled, $\alpha_M = 0.8$ $T$ -dependent $C_{ave}$ sublimates
Boiarciuc [34]	Kinetically controlled, $\alpha_M = 0.8$ $T$ -dependent $C_{ave}$ sublimates
Dreier–Bockhorn [38]	Kinetically controlled, $\alpha_M = 1$ Only $C_3$ sublimates, $p_{vap}$ by Antoine equation
Dreier–Roth [30]	Kinetically controlled, $\alpha_M = 1$ Only $C_3$ sublimates
Dreier–Schittkowski [35]	Kinetically controlled, $\alpha_M = 1$ Only $C_3$ sublimates
Hadef et al. (DLR) [44]	Kinetically controlled, $\alpha_M = 0.8$ $T$ -dependent $C_{ave}$ sublimates
Kock–Roth [11, 30, 52, 53]	Kinetically controlled, $\alpha_M = 1$ Only $C_3$ sublimates
Liu (NRC) [33, 34, 46]	Kinetically controlled, $\alpha_M = 0.9$ $T$ -dependent $C_{ave}$ sublimates
Michelsen (Sandia) [39]	Kinetically controlled, except near sublimation $T$ $\alpha_M(C_1, C_2) = 0.5$ , $\alpha_M(C_3) = 0.1$ , $\alpha_M(C_4–C_{10}) = 10^{-4}$ $C_1–C_{10}$ sublime

TABLE 4 Model treatment of sublimation rates

**2.3.3 Dreier–Bockhorn.** This model was implemented by Dreier according to a recent description by Lehre et al. [38]. It uses a Rayleigh approximation with  $m = 1.90\text{--}0.55$  i [51] for absorptive heating, radiative cooling, and signal prediction. It assumes a free-molecular flow regime with  $\alpha_T = 0.2$  for conductive cooling rate calculations. Sublimation rates are calculated using the Antoine equation for vapor pressures, assuming that the sublimation process is kinetically controlled ( $\alpha_M = 1$ ). The cluster velocity away from the surface is calculated as

$$U = \alpha_M \left( \frac{RT}{2\pi W} \right)^{0.4}, \quad (1)$$

where  $R$  is the universal gas constant,  $T$  is the temperature, and  $W$  is the molecular weight of sublimed clusters. The exponent of 0.4 accounts for the non-ideality of the ambient gases and desorbed clusters (most of the other models use a value of 0.5). According to Lehre et al. [38], this modification is numerically equivalent to using an average molecular weight of sublimed carbon clusters  $C_{\text{ave}}$  instead of assuming that only  $C_3$  sublimes.

**2.3.4 Dreier–Roth.** This model was reconstructed by Dreier from a description given by Roth and Filippov [30], Filippov et al. [11], and Starke et al. [52] and is nominally the same as the Kock–Roth model (see below).

**2.3.5 Dreier–Schittkowski.** This model has been implemented by Dreier as described by Schittkowski et al. [35]. Absorption and radiation are calculated using the Rayleigh approximation with  $m = 1.90\text{--}0.55$  i [51]. Conductive cooling is calculated assuming a transition regime according to McCoy and Cha [48] with  $\alpha_T = 0.9$  and a temperature-dependent thermal conductivity. Sublimation rates are calculated assuming that sublimation is kinetically controlled and only  $C_3$  sublimes with  $\alpha_M = 1$ .

**2.3.6 Hadef.** Absorptive heating, radiative cooling, and signal prediction are calculated with a Rayleigh approximation where  $E(m)$  is wavelength dependent. These terms are calculated in the same way as in the Boiarciuc model;  $E(m)$  is taken from data and analyses presented by Krishnan et al. [50] and fitted by Snelling et al. [41] and is given by  $E(m) = 0.232 + \lambda \times 1254.6$  for  $\lambda$  in cm. Conductive cooling rates are assumed to be in the free-molecular flow regime at low pressure and approximated with the transition-regime expression from McCoy and Cha [48] at higher pressure ( $\alpha_T = 0.3$ ). The transition from the free-molecular flow regime to the transition regime is assumed to occur when the Knudsen number drops below  $5\sqrt{\gamma\pi/2}$ , where  $\gamma$  is the heat-capacity ratio. Temperature-dependent densities and heat capacities are used to calculate the particle's internal energy. Sublimation rates are assumed to be kinetically controlled, include a temperature-dependent average mass and enthalpy of formation for the sublimed clusters, and use (1) with  $\alpha_M = 0.8$  to calculate the velocity of clusters leaving the surface.

**2.3.7 Kock–Roth.** This model [53] is based on a model originally described by Roth and Filippov [30] and Filippov et

al. [11] and more recently by Starke et al. [52] and Kock et al. [23]. It is generally used to calculate a cooling rate after reaching a maximum temperature that is determined experimentally and used as input into the model. Radiative cooling and signal prediction is based on a Rayleigh approximation with  $m = 1.82\text{--}0.59$  i [54]. In this study the Rayleigh approximation is also used to calculate a heating rate during the laser pulse. Conductive cooling is calculated assuming a free-molecular flow regime at low pressure ( $\alpha_T < 1$ ), a transition regime at intermediate pressure ( $\alpha_T = 0.23$ ), and a continuum regime at high pressure. Sublimation rates are calculated with the assumptions that sublimation is kinetically controlled and only  $C_3$  sublimes ( $\alpha_M = 1$ ). The effects of aggregation on the conductive cooling rate are accounted for by assuming an equivalent heat-transfer size for the aggregate.

**2.3.8 Liu.** This model is a modified version of the model described by Snelling et al. [33], Smallwood et al. [34], and Liu et al. [46]. It uses a temperature-dependent specific heat to calculate the internal energy of the particle. It uses the Rayleigh–Debye–Gans (RDG) approximation to calculate absorptive heating rates, radiative cooling rates, and LII signals with  $E(m) = 0.4$ . Conductive cooling calculations use a transition-regime approximation with a Fuchs approach based on recent work by Filippov and Rosner [55] and  $\alpha_T = 0.37$ . The effects of aggregation are included in this calculation by the assumption of an equivalent heat-transfer size. Aggregation is not accounted for in the calculations of sublimation rates, which are assumed to be kinetically controlled and include a temperature-dependent average mass and enthalpy of formation for the sublimed clusters ( $\alpha_M = 0.9$ ).

**2.3.9 Michelsen.** This model is a modified version of the model described by Michelsen [39, 40]. As with the original version, it includes particle annealing and uses temperature- and phase ( $\varphi$ )-dependent specific heat and density to calculate the internal energy of the particle. It accounts for the effects of aggregation on the optical properties by using the RDG approximation instead of the Rayleigh approximation [48] in the calculation of absorption and emission but does not account for the effects of aggregation on conduction or sublimation. The RDG approximation used yields different wavelength dependences for the absorption cross section  $\sigma_\lambda$  and emissivity  $\varepsilon_\lambda$  than estimated with the Rayleigh approximation with a constant value of  $m$ . The phase dependence is also included in the calculation of the optical properties. The model accounts for sublimation and convective and diffusive transport of carbon clusters  $C_1\text{--}C_{10}$  from the surface. Thus, the net mass and enthalpy of formation are calculated separately for each cluster species as a function of temperature. This model assumes free-molecular flow for conductive cooling at atmospheric pressure and uses the transition-regime approximation from McCoy and Cha [48] with temperature-dependent heat capacities and thermal conductivity at higher pressures ( $\alpha_T = 0.26$ ). It includes heating and mass loss by oxidation and cooling and mass loss by photodesorption. The original version of the model was optimized for 532-nm absorption. The version presented here also treats heating by 1064-nm radiation, in which case the photodesorption proceeds via a three-photon transition. This version of the model accounts

for the energy acquired by the particle during multi-photon absorption at 532 and 1064 nm. It also includes cooling by thermionic emission using a Richardson–Dushman approximation [31, 56].

## 2.4 Results and discussion

We will show selected results from the model comparisons to highlight some of the features of the different models and discuss sensitivities of the models to particular mechanisms. Starting with a low-fluence case, Fig. 1 shows temporal LII-intensity profiles for 532-nm (Case 1) and 1064-nm (Case 7) excitation. The calculations for 532- and 1064-nm excitation give similar results for each model, and we will focus on the calculations for 532 nm for the rest of the discussion. The comparison shown in Fig. 1 demonstrates large differences between the models. At these fluences the decay rates are determined predominantly by conductive cooling rates. Despite the similarities in how the models handle conductive cooling (i.e. more than half of the models assume a free-molecular flow regime at 1 bar), the differences in the decay rates are significant. One reason for these differences is related to the range of values used for the

thermal accommodation coefficient. A larger value of  $\alpha_T$  will lead to a more efficient loss of energy to the surrounding atmosphere and, hence, a faster decay. The Dreier–Roth model, for example, uses the largest value of  $\alpha_T$  and predicts a significantly faster decay than predicted by the other models.

Because the conductive cooling rate depends on the difference in temperature between the particle and the ambient atmosphere, differences in conductive cooling rates will be emphasized at lower ambient temperatures. Figure 2 shows comparisons at an ambient temperature of 300 K (Case 3), expanded in the time domain by a factor of four relative to Fig. 1. All of the models demonstrate faster decay rates at lower temperatures, as expected, and ordering is generally preserved, i.e. the models with the slowest decay rates at 1800 K also have the slowest decay rates at 300 K. The conductive cooling rate also increases with increasing pressure, and behavior similar to that observed at lower temperatures is observed at higher pressures. Figure 2 shows comparisons at an ambient pressure of 10 bar (Case 5). Several of the models calculate conductive cooling rates differently at high pressure, which may contribute to some of the reordering of the models with respect to changes in decay rates with pressure.

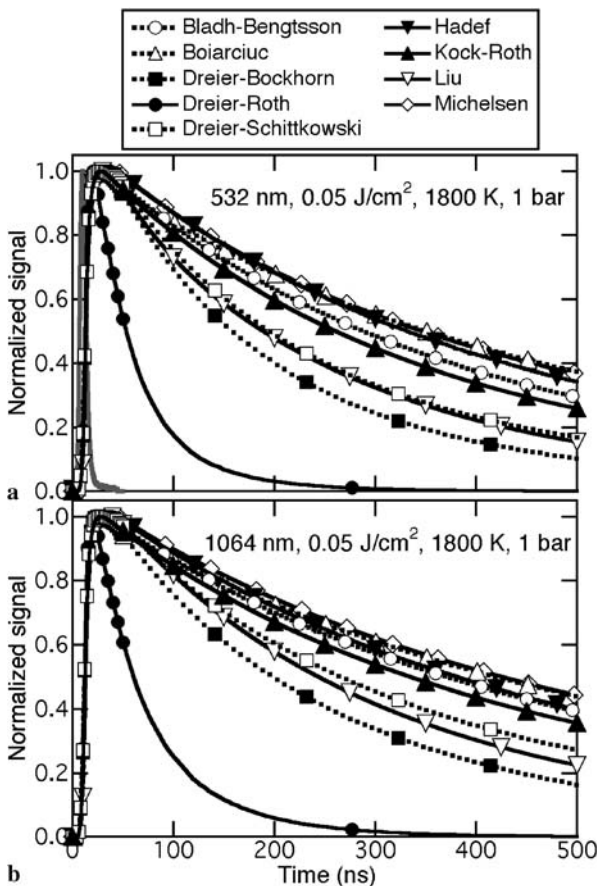


**FIGURE 1** Comparison of modeled low-fluence LII temporal profiles. Model predictions are shown for a laser fluence of  $0.05 \text{ J/cm}^2$  at an ambient temperature of 1800 K and a pressure of 1 bar and excitation wavelengths of (a) 532 nm and (b) 1064 nm. The models are identified by line type and symbol in the legend at the top. The laser profile is represented by the solid gray curve. Each modeled profile has been normalized to unity at the maximum point on the curve

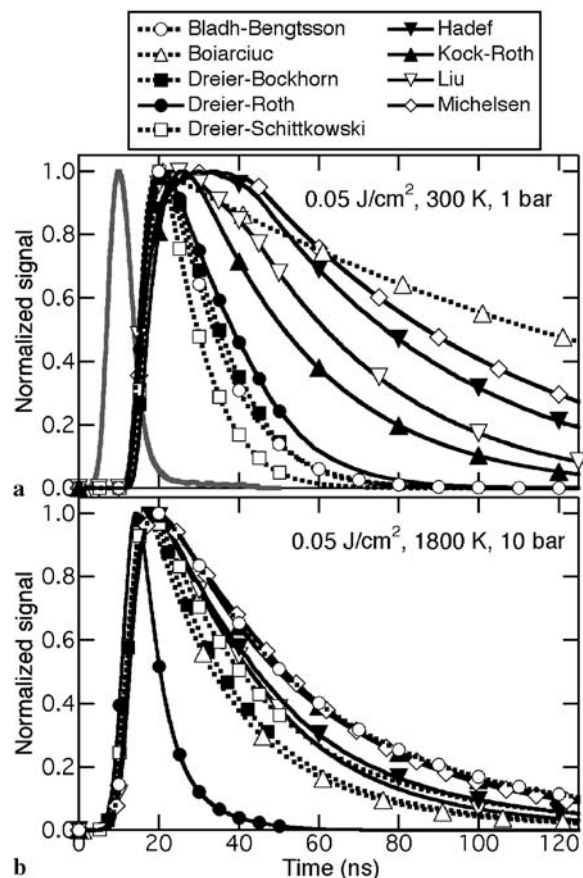


**FIGURE 2** Comparison of modeled LII temporal profiles highlighting pressure and temperature effects. Model predictions are shown for a laser fluence of  $0.05 \text{ J/cm}^2$  at an excitation wavelength of 532 nm and ambient temperature and pressure of (a) 300 K and 1 bar and (b) 1800 K and 10 bar. The models are identified by line type and symbol in the legend at the top. The laser profile is represented by the solid gray curve. Each modeled profile has been normalized to unity at the maximum point on the curve

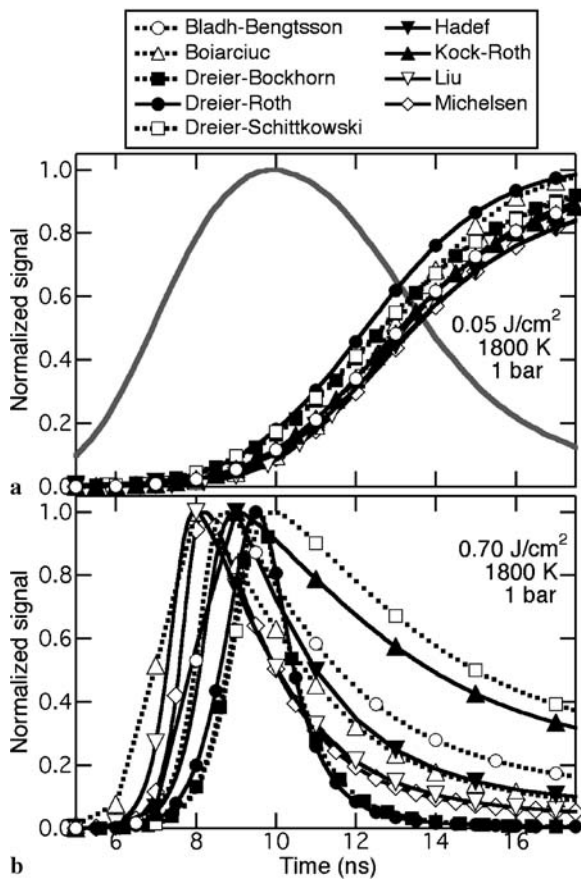


**FIGURE 3** Comparison of modeled LII temporal profiles highlighting differences in predicted rise times. Model predictions are shown for an excitation wavelength of 532 nm and ambient temperature of 1800 K and pressure of 1 bar and laser fluences of (a)  $0.05 \text{ J/cm}^2$  and (b)  $0.70 \text{ J/cm}^2$ . The models are identified by line type and symbol in the legend at the top. The laser profile is represented by the solid gray curve. Each modeled profile has been normalized to unity at the maximum point on the curve

Another factor that affects the decay rates at these fluences is the peak temperature the particle reaches during the laser pulse, which will depend on the absorptive heating rate. At low fluences larger absorption cross sections lead to higher peak temperatures and slightly faster decay rates. The absorptive heating rate also controls the initial rise time of the LII signal. Figure 3 shows temporal profiles for 532-nm excitation at low fluence (Case 1) and high fluence (Case 2) expanded in the time domain by a factor of 40 relative to Fig. 1. Despite the similarity in how most of the models treat the absorptive heating rate, the spread in the leading edge of the calculated temporal profiles is significant. This spread likely reflects the differences in the value of the index of refraction used. The range of absorptive heating rates is difficult to assess, however, because each of the models is scaled to unity at the peak. Comparing calculated temperatures would provide better information about the relative rates of heating and cooling.

Signal decay rates at the higher fluences are predominantly determined by rates of particle-volume reduction by sublimation. As with the low-fluence cases, there is a large spread in the calculated temporal profiles, even for models that nominally treat the sublimation in the same way, e.g. Dreier-Roth and Kock-Roth. In this case it would be useful

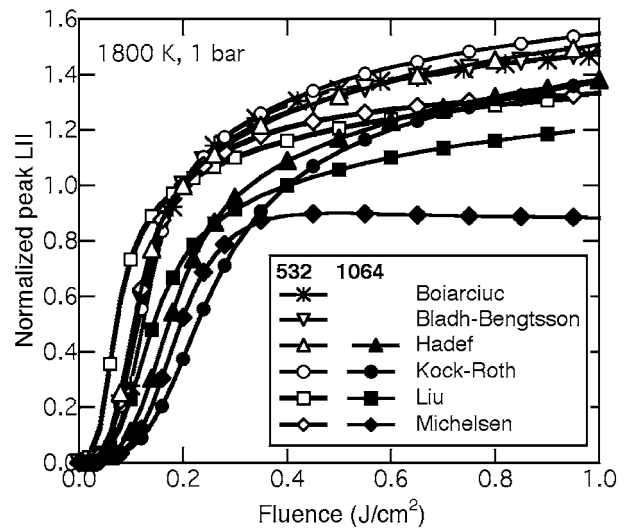


**FIGURE 4** Fluence dependence of modeled LII signal magnitudes. The peaks of the modeled LII temporal profiles are plotted as a function of fluence for excitation wavelengths of 532 nm (open symbols) and 1064 nm (closed symbols) and ambient temperature of 1800 K and pressure of 1 bar. The 532-nm results for each model are normalized to unity at  $0.2 \text{ J/cm}^2$ . The same scaling is used for the 1064-nm results. The models are identified by symbols in the legend

to compare the calculated energy and mass loss from sublimation directly.

Some differences between the models are reflected in the fluence dependence of the peak of the temporal profiles, shown in Fig. 4. Despite differences in the temporal profiles, the Bladh-Bengtsson, Boiarciuc, and Kock-Roth models give similar results for the relative magnitudes as a function of fluence. The Liu model gives relatively higher signal at the low fluences; this behavior may result from a larger absorption cross section, which is consistent with the relatively fast rise times for the temporal profiles from this model shown in Fig. 3. The Michelsen model has less fluence dependence at the higher fluences ( $> 0.2 \text{ J/cm}^2$ ) than the other models; this lack of fluence dependence is attributable to the inclusion of the photodesorption term [39].

## 2.5 Conclusions

This comparison of nine LII models highlights the uncertainties in our understanding of the mechanisms that influence LII signals. Given the large differences between the results from different models, considerable work needs to be done to narrow these uncertainties. This work should include future model comparisons and sensitivity analyses, additional laboratory measurements of critical input parameters, and tests of the models under a wider range of conditions and with more detailed experimental results.

Several of the models presented here are reproduced from descriptions given in the literature. One common problem with recreating models from the literature is a lack of detail or errors in the description given in the original papers. In these situations assumptions often need to be made about how mechanisms are to be implemented. Such assumptions may lead to differences in model behavior from that of the original model. In the future, emphasis should be placed on identifying

differences in implementation of particular mechanisms and clarifying ambiguities in model descriptions that appear in the open literature.

## 2.6 Future model intercomparisons

LII models incorporate complex and competing mechanisms that have a strong influence on predicted signal magnitudes and evolution. In order to understand the roots of the differences between these models, comparisons will need to be simplified and made on a more fundamental level. With this goal in mind, we have compiled a list of model scenarios for future comparisons. (1) Such comparisons should involve tests of the equation-solving methodology, such as running the same model (e.g. the Melton model [28]) using the same coefficients. (2) To ensure that similar treatments of mechanisms give similar answers, different models could be run with the same coefficients (e.g. refractive index, mass and temperature accommodation coefficients, and heats of formation of carbon clusters). (3) Model comparisons could be made by focusing on temperature and diameter predictions corresponding to the LII signal predictions, which would give more direct information about heating, cooling, and mass loss. (4) Even more detailed information about model performance could be gained by focusing on comparisons of the calculated contributions to the energy flux from each mechanism. (5) To isolate the influence of the cooling mechanisms from the absorptive heating process, temperature evolution could be calculated using an initial temperature as input into the models while excluding the absorptive heating term.

## 2.7 Experimental input

LII models incorporate a considerable number of parameters. Many of the parameters to which the models are sensitive have large uncertainties. We have compiled a list of parameters that need further laboratory investigation. This list includes (1) temperature- and wavelength-dependent optical properties of soot, (2) temperature-dependent thermal accommodation coefficients in different gases, (3) mass accommodation coefficients for carbon clusters on particle surfaces, (4) internal state distributions of desorbed or sublimed  $C_2$ , (5) propensities for  $C_3$  desorption or sublimation, and (6) aggregation effects on optical properties, conductive cooling rates, and sublimation rates.

## 2.8 Future model comparisons with experimental results

To test the validity of LII models, these models need to be compared to a wide range of detailed experimental data. We have compiled a list of experimental observations that would aid in model validation. This list includes (1) LII data recorded at low gas temperatures, (2) LII data recorded at high pressures, (3) spectrally- and temporally-resolved emission and/or temperature temporal profiles derived from these data, (4) LII temporal profiles recorded with higher time resolution, and (5) single-particle LII data.

## 3 Experimental issues

This section deals with experimental techniques used to generate and detect LII signals. Different approaches

are used depending on the objective of a given experiment. In general, the two main objectives are the determination of soot volume fractions, either one- or two-dimensional, and the measurement of primary particle sizes. The accuracy of the data obtained is significantly influenced by many experimental parameters, e.g. excitation and detection wavelengths, laser fluence and spatial beam profile, temporal detection issues, and calibration methods.

### 3.1 Excitation and detection wavelengths

Soot is a broad-band absorber and, although the absorption cross section increases with decreasing wavelength, in principle any wavelength in the visible or IR regions can be used to heat the particles for LII detection. Ultraviolet excitation wavelengths of 266 and 355 nm have been shown to generate LII [57], but shorter UV wavelengths preferentially promote photodissociation instead of particle heating [58].

Nd:YAG lasers are frequently used for LII excitation because these lasers are generally reliable, readily available, and provide high-power pulses with typical pulse durations of 8–15 ns. The fundamental (1064 nm) or second harmonic (532 nm) are most often used for LII applications. However, care must be taken with the excitation and detection strategy to avoid non-LII signal interferences. Typically, excitation with 1064 nm results in less interference than excitation with 532 nm or shorter wavelengths for the following three reasons:

- At longer excitation wavelengths, the generation of electronically excited  $C_2$  fragments is less pronounced. Emissions from the  $C_2d^3\Pi_g \rightarrow a^3\Pi_u$  Swan bands have been reported to interfere with the LII signal at high laser power densities [59], and even emissions from OH and O atoms have been observed with 532-nm excitation [5].  $C_2$  Swan-band emissions can also be observed with 1064-nm excitation at high laser fluences, especially with non-uniform beam profiles that provide high local fluence [5]. Excited  $C_2$  emission is short-lived, however, and the interference occurs only during the laser pulse and decays quickly thereafter.
- Laser-induced fluorescence (LIF) of polycyclic aromatic hydrocarbons (PAH) is induced with excitation in the visible and the UV (see [60–64] and references therein). PAH are common soot precursors in flames, and their fluorescence extends over a large spectral range in the visible. It is therefore not easily separated with detection filters from the LII signal. With increasing laser fluence the contribution of PAH interference increases and can be up to 80% with 532-nm excitation in diffusion flames as shown in Fig. 5. On the other hand, simultaneous excitation at 266 nm and 1064 nm has been used to simultaneously detect PAH LIF and LII in laminar and turbulent diffusion flames [65–74]. It should be noted that PAH fluorescence is short-lived at elevated temperatures [62, 63], and the interference occurs predominantly during the laser pulse and decays quickly thereafter.
- Elastically scattered light is very strong in sooting flames. If the LII signal is detected in the visible, elastically scattered light at 532 nm might not be entirely blocked by the detection filters causing a perturbation to the LII signal

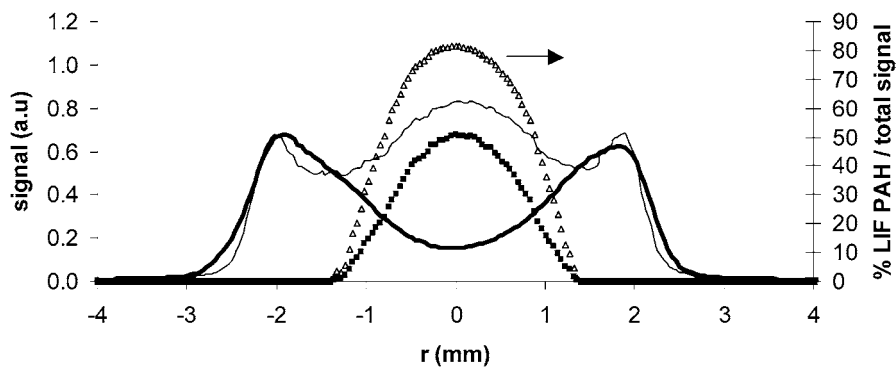


**FIGURE 5** Comparison of the intensities of the PAH and soot emission signals upon 532-nm excitation for a 20-ns gate at the peak of the temporal LII signal in a sooting diffusion flame ( $f_{v,max} = 160$  ppb), HAB = 13 mm. *Solid line*: LII measurement at  $\lambda_{ex} = 532$  nm,  $\lambda_{det} = 650$  nm, *bold solid line*: LII measurement at  $\lambda_{ex} = 1064$  nm/ $\lambda_{det} = 410$  nm shown for comparison (signal/7.2), *squares*: PAH LIF from two-color LII and *triangles*: percentage of signal due to PAHs at  $\lambda_{ex} = 532$  nm/ $\lambda_{det} = 650$  nm. The PAH profile has been smoothed in the lateral wings for convenience. Reproduced from [107]

at early times. In contrast, infrared scattering cross sections are much smaller than visible cross sections, making IR scattered light easier to discriminate against when IR excitation and detection in the visible are employed. Additionally, many photodetectors used in LII have weak or no response at 1064 nm, limiting the interference at this wavelength. However, in cases when one wants to perform measurements of both LII and elastic light scattering, the combined use of 532 nm will be favored over the use of 1064 nm.

In general, any refractory or metallic particle, such as soot, that absorbs laser radiation will incandesce – resulting in LII. The individual primary particles are spherical and typically 50 nm or less in diameter and thus satisfy the Rayleigh criterion that  $\pi d_p/\lambda < 0.3$  for visible wavelengths. Whereas the interaction of the isolated primary particles with light can be described by Rayleigh theory, that of the much larger aggregates cannot. The absorption efficiency and the emissivity,  $\varepsilon(\lambda)$ , are both wavelength dependent and equal. The emissivity is now a function of particle size rather than the intrinsic property of a bulk material. RDG/PFA (Rayleigh–Debye–Gans/poly-disperse fractal aggregate) theory predicts that the absorption of light by a soot aggregate is the product of the absorption cross section of a single primary particle by the number of individual primary particles making up the aggregate. Direct numerical simulation of aggregate interaction with light [75–78] indicates that the errors due to the RDG/PFA theory of aggregate absorption are less than 10% even for soot aggregates that are as large as 300–500 primary particles for values of  $\pi d_p/\lambda < 0.5$ . It is this RDG/PFA limit that is significant for aggregated soot nanoparticles [46], not the Rayleigh limit frequently mentioned in the literature. If models are compared with experimental LII signals, particles and the laser wavelength in the experiment should match the RDG/PFA condition. Second, the assumption in two-color LII (explained in Sect. 3.5) that the peak particle temperature is independent of the aggregate size is also only valid in the RDG/PFA limit. This condition is more likely to be fulfilled for 1064 nm than for 532 nm.

The particle incandescence is spectrally very broad, and LII-signal detection can be performed over a wide range of wavelengths. Experimental and theoretical work have shown [12, 79] that detection at longer wavelengths minimizes the influence of a variation in particle size and ambient-gas temperature. However, in most practical environments detection in the blue around 400 nm is preferred to improve the

discrimination of LII signal against flame luminosity. In any case, detection of high-fluence LII should be avoided at wavelengths where interference from  $C_2$  emission is expected, i.e. in the  $C_2$  Swan bands at 473 nm ( $\Delta v = +1$ ), 516 nm ( $\Delta v = 0$ ), 563 nm ( $\Delta v = -1$ ), and 618 nm ( $\Delta v = -2$ ). The interferences from  $C_2$  or other species might change with increasing ambient pressure because of efficient quenching of the excited fragments. On the other hand, number densities will increase with increasing pressure that can cause an increase in interferences from  $C_2$ . In [80] an LII spectrum at 15 bar is presented; this spectrum does not show any narrow-band LIF interference in the range between 280 and 520 nm with 532-nm excitation. Still, more detailed investigations are necessary about interferences in LII at elevated pressure.

For two-color LII, an additional consideration must be made in that the two wavelengths must be selected to provide an acceptably accurate and precise measure of the particle temperature. For such measurements the range of temperatures to be considered is wide, ranging from peaks of 3000 K (low fluence) to 4500 K (high fluence) decaying down to 2000 K or lower (depending on the instrument sensitivity). In addition, there is a wide variation in the spectral sensitivity of available photodetectors. Care must therefore be taken in the selection of the two wavelengths to maximize the integrity of the temperature measurement.

### 3.2 Laser fluence

The laser fluence has a large impact on LII-signal intensities. Temporally integrated and time-resolved LII signals depend strongly on fluence since different heat-loss mechanisms dominate at different laser fluences. The absorption cross section is inversely proportional to wavelength. To a first approximation, ignoring any variation in the absorption function  $E(m)$  with wavelength, excitation at 1064 nm requires twice the energy needed for 532-nm excitation to heat the particles to the same temperature.

At low fluences the peak LII intensity rises monotonically with laser fluence as peak particle temperatures increase. For a true black body (emissivity of one), integrating the Planck function over all wavelengths yields an expression that is proportional to  $T^4$ . However, a Rayleigh particle is not a black body, and the emissivity is usually assumed to be inversely proportional to wavelength. Multiplying the Planck function by an emissivity with a  $1/\lambda$  dependence and integrating over all wavelengths yields an expression for the radiative emission (and, hence, signal) that is proportional to  $T^5$ . With increasing

laser fluence soot sublimation during the laser pulse increases and evaporative cooling and mass loss cause the maximum LII signal to remain constant as shown in Fig. 6. At fluences above  $0.2 \text{ J/cm}^2$  for 532-nm excitation in a flame, the peak signal is nearly fluence independent for an 8-ns-long laser pulse with a homogeneous top-hat spatial profile [39, 40]. When the signal is gated, i.e. it is temporally integrated over the gate width, the signal also increases with increasing fluence at low fluences. At fluences just above  $0.2 \text{ J/cm}^2$  for 532-nm excitation and above  $\sim 0.3 \text{ J/cm}^2$  for 1064-nm excitation the gated LII signal from soot in flames is frequently observed to be nearly independent of fluence [4, 10, 16, 27, 79, 81]. Excitation laser fluences within this plateau region have been preferred in soot volume fraction measurements in practical applications with strong laser attenuation or laser power fluctuations. With further increasing laser fluence, sublimation significantly reduces the soot particle size and volume fraction, which results in a reduction in gated LII signals when a homogeneous top-hat laser beam profile is used [7, 40, 82]. A typical excitation curve is shown in Fig. 7 for a top-hat beam profile. With a two-dimensional Gaussian laser beam, gated LII signals continu-

ously increase with laser fluence [9, 13, 37, 83] as shown in Fig. 7. With a one-dimensional Gaussian sheet beam profile, an extended plateau region is observed [4, 5, 7, 21, 33]. In this case, the decrease in gated LII signal intensity due to soot sublimation in the center of the beam is approximately compensated by an increase in gated signal intensity in the wings of the beam where the sublimation threshold has not yet been reached. In some practical applications where soot volume fraction measurements were attempted in strongly sooting environments with extreme laser attenuation, this coincidental canceling of two artifacts has been exploited. These effects are discussed further in Sect. 3.4.

When sublimation occurs various soot fragments evaporate from the particle surface. They are assumed to range from  $C_1$  to  $C_7$  dependent on the particle temperature [49]. Models often assume either  $C_3$  as the major species or a composition of  $C_1$ – $C_7$  to evaporate. To date, experiments with spectrally resolved detection of the LII signal have shown emissions from electronically excited  $C_2$  fragments [5, 59]. Although no experimental results have been reported on luminescence from larger carbon species, the current results do not rule out their presence in the electronic ground or excited states. For example, emission from  $C_3$  has been observed following 532-nm laser irradiation of graphite under vacuum or in rare-gas atmospheres [84–87], but  $C_3$  radiative emission may be quenched under higher pressures of molecular species. Additionally, ground-state  $C_2$  has been detected by laser-induced fluorescence from laser-vaporized soot [59].

Understanding the sublimation is further complicated by additional uncertainties in physical parameters such as the vapor pressure and heat of formation of the carbon species [34], which results in significant uncertainties in modeled LII signals [40]. Intense laser radiation can change the properties of soot even below the sublimation threshold, resulting in structural and morphological changes. Vander Wal et al. [88] have shown transmission electron microscopy (TEM) images of laser-heated soot extracted from a flame. While there were no significant changes to the soot particles observed at a fluence of  $0.15 \text{ J/cm}^2$  with 1064-nm excitation, at  $0.3 \text{ J/cm}^2$  the structure of soot changed to hollow particles. At fluences of  $0.6 \text{ J/cm}^2$  ribbons of several carbon layers appeared at the perimeter of the particles. At a fluence of  $0.9 \text{ J/cm}^2$  considerable material loss from the soot aggregate was observed. All these effects may have a strong influence on the optical properties of soot, which could have a substantial effect on the absorption and emission rates important for LII [39].

If experiments at different laser fluences are performed, attention should be paid to the way in which the laser energy is changed. As will be discussed in Sect. 3.4, the spatial laser beam profile has a large impact on the LII signal. In the case of a Q-switched Nd:YAG laser the energy can be changed by changing the high voltage of the flashlamps (if a flashlamp-pumped laser is used) or by changing the timing of the Q-switch. Both strategies affect the beam profile and might therefore lead to erroneous results. Beam attenuation without alteration of the spatial profile can be more easily accomplished with the use of a half-wave plate (to rotate the plane of polarization) in combination with a thin-film polarizer (to pass a single polarization at the excitation wavelength). In this case care must be taken to ensure that stress

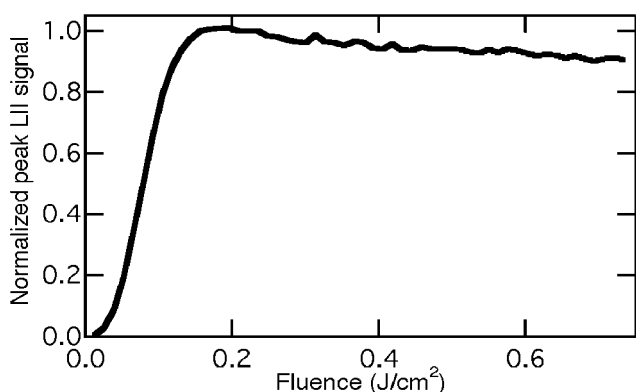


**FIGURE 6** Fluence dependence of the peak LII signal for time-resolved measurements. Values are normalized to unity at  $0.2 \text{ J/cm}^2$ . Measurements were made at 532 nm with a top-hat beam profile from an injection-seeded Nd:YAG laser and fast photodiode under the flame conditions given for the Santoro burner in Table 7

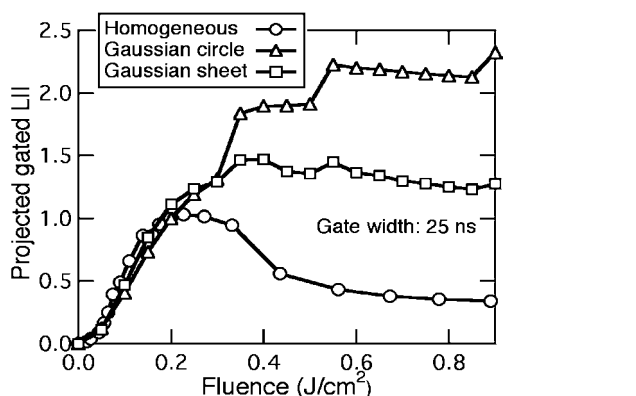


**FIGURE 7** Fluence dependence of LII signal as a function of laser beam spatial profile for top-hat (homogeneous), 1D Gaussian (*Gaussian sheet*), and 2D Gaussian (*Gaussian circle*) profiles [40]. The results for Gaussian profiles were simulated by summing the fluence-dependence measurements from a top-hat profile (*circles*) weighted by a Gaussian distribution in one dimension (*squares*) or two dimensions (*triangles*). Gated detection was simulated by integrating the time-resolved signal over the first 25 ns

birefringence within the gain medium of the laser does not produce an output with significant components to the off polarization. Stress birefringence is most likely to affect the fundamental output from high-power Nd:YAG lasers. Under these conditions the laser spatial and temporal profiles will be substantially different for the off polarization, which is preferentially passed through the polarizers at low fluences [89]. Such problems can be corrected with an additional thin-film polarizer used to block the stress-induced off polarization at the output of the laser. Alternatively, a dielectrically coated attenuator (angle-dependent partial reflection of the beam) can be used to attenuate the laser beam.

For soot volume fraction measurements, the gated LII signal is proportional to the soot volume fraction. This relation is valid for a wide range of laser fluences as shown by Vander Wal and Jensen [82] in laminar diffusion flames but has not been explored thoroughly for all laser beam profiles. In practical applications with strong laser attenuation, e.g. in diesel engines, high-excitation laser fluences within the plateau region have been used in soot volume fraction measurements because the LII signal is considered more or less independent of laser fluence (and, hence, only weakly affected by laser attenuation) [90–92]. However, these studies have not systematically investigated the influence of variations in the ambient-gas temperature, severe laser attenuation, drift in the laser energy, or the quantity of condensed species on the surfaces of the soot particles.

For LII-based particle-size measurements, the high-fluence approach, however, is detrimental. In this case, sublimation should be avoided because models used for the data evaluation do not describe the sublimation correctly. At the LII workshop, general agreement was found on the use of low laser fluences for soot particle sizing in order to avoid sublimation. For LII particle sizing ‘low fluence’ typically means  $< 0.2 \text{ J/cm}^2$  [41, 93] with 1064-nm excitation in flames. Problems might occur in strongly sooting environments when the laser beam is heavily attenuated. In these cases, a careful choice of the laser fluence is required to make sure that it is below the sublimation threshold while the signal-to-noise ratio is still acceptable.

Previous studies have indicated that soot particle volumes can be reduced by as much as 80%–90% for 1064-nm excitation at laser fluences of  $0.47\text{--}0.61 \text{ J/cm}^2$  [94] and by 50%–60% for 532-nm excitation at similar fluences [95]. Size reduction does not appear to be significant at fluences below  $0.1 \text{ J/cm}^2$  for 1064-nm excitation [94]. The threshold for volume reduction appears to be in the range of  $0.12\text{--}0.2 \text{ J/cm}^2$  for 532-nm excitation [95, 96]. With two-color LII, low fluences can be employed to determine soot volume fraction [20, 97] without relying on a plateau region resulting from the coincidental cancelation of artifacts, and avoiding significant sublimation and interference from  $\text{C}_2$  emission. This technique avoids the reduction in particle volume and primary particle diameter that occur at high fluence. This is achieved by time-resolved measurements of the particle temperature.

### 3.3 Determination of $E(m)$

Large variability has been demonstrated in measurements of soot refractive index. Furthermore, the optical

parameter of direct interest for LII is the soot absorption function  $E(m)$ . References often chosen for refractive-index data rely on analyses that are now believed to be incorrect. As an example, the frequently used data of Chang and Charalampopoulos [54] was derived from conventional and dynamic light scattering coupled with a dispersion relationship. In doing this, they ignored aggregate formation, treated the scattering by Mie theory, and used a dispersion relationship based on graphite. All of these assumptions are questionable, and hence the validity of these refractive-index data is suspect. For details of potential problems with refractive-index data, see Faeth and co-workers [98] and references therein.

To estimate  $E(m)$ , it is sufficient but not necessary to know the refractive index  $m$ . There is a considerable amount of published work where the spectral dependence of  $E(m)$  has been measured by a combination of light extinction, with correction for light scattering, and gravimetric determination of soot concentration [50, 98–102]. In general, these references show that  $E(m)$  is  $0.3 \pm 0.06$  and is approximately constant throughout the visible to near-IR region of the spectrum, as illustrated in Fig. 8. This result is consistent with the conclusion from flame spectral emission coupled with coherent anti-Stokes Raman scattering (CARS) temperature measurements [103].

As noted in Sect. 2.3, there exists a possibility that the laser heating of the particles may induce a phase change, which in turn could have an impact on  $E(m)$ . The phase change has been modeled to be more rapid and complete at higher fluences [39], a further reason to avoid high-fluence LII. Experiments have been performed at low fluence, fitting  $E(m)$  to

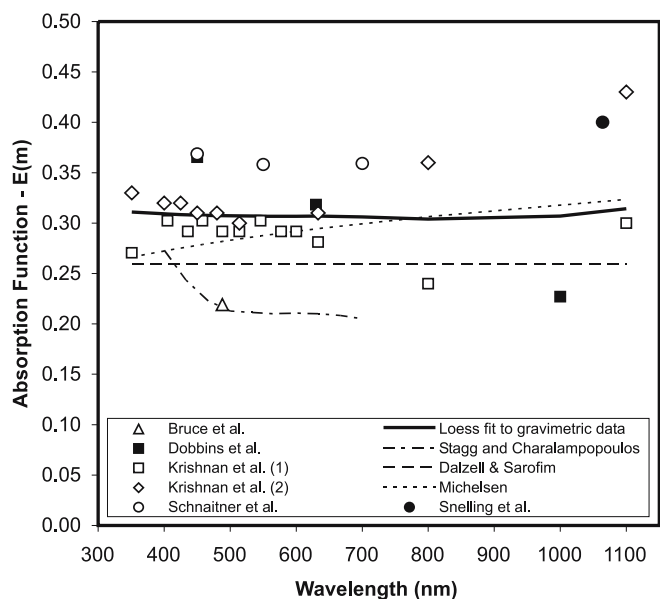


**FIGURE 8** Absorption function determined for flame and diesel soot over the UV-VIS-NIR spectrum. The results shown are (a) determined from comparisons of in situ optical to gravimetric measurements (empty triangles – Bruce et al. [101], filled squares – Dobbins et al. [102], empty squares – Krishnan et al. [98], empty diamonds – Krishnan et al. [50], empty circles – Schnaitner et al. [100]); (b) Loess fit to all of the in situ measurements (solid line); (c) ex situ measurements of effective refractive index (dash-dot line – Stagg and Charalampopoulos [142]); fits to refractive-index data (dashed line – Dalzell and Sarofim [47], dotted line – Michelsen [39]); and fit to low-fluence LII peak temperature (Snelling et al. [41])

reproduce the experimentally derived peak temperature from two-color pyrometry [41]. Under the assumption of constant  $E(m)$  this study results in a value of  $E(m) = 0.4$  at a laser wavelength of 1064 nm. Assuming a linear increase of  $E(m)$  with wavelength, the resulting  $E(m)$  value is 0.42 for the same conditions.

Beyer and Greenhalgh [104] have demonstrated another novel method for the estimation of  $E(m)$ . With low-fluence LII in vacuum, in the absence of conductive and sublimation heat loss, elevated particle temperatures are maintained for tens of microseconds, as cooling is primarily due to radiative heat loss [104]. Under these conditions,  $E(m)$  can in principle be determined from the relation

$$E(m) = \frac{h^4 c^3}{1194\pi^2 k^5} \frac{\rho_s(T) c_s(T)}{T^5} \frac{dT}{dt}, \quad (2)$$

where  $h$  is the Planck constant,  $c$  is the speed of light,  $k$  is the Boltzmann constant,  $\rho_s$  is the particle density,  $c_s$  is its specific heat,  $T$  represents temperature, and  $t$  represents time. Initial experiments under vacuum conditions indicate results that are consistent with  $E(m) = 0.4$ .

### 3.4 Laser profile

The laser spatial and temporal profiles have a marked impact upon the LII signals that are generated.

**3.4.1 Temporal profile.** The laser temporal profile has received little attention, as most researchers are currently employing similar Nd:YAG lasers with approximately 7–10 ns FWHM pulse durations. Furthermore, it is difficult to vary the laser temporal profile in a well-controlled way in order to determine the effect of the temporal behavior. Most researchers claim that the temporal profile follows a Gaussian behavior, although those that provide measured profiles show a skewed shape with a somewhat longer tail, lasting up to 30 ns [33].

When soot is heated with a 532-nm picosecond laser, the temporal behavior of the LII signal is qualitatively similar to that resulting from excitation with a nanosecond laser. In this issue Michelsen [105] presents time-resolved LII using a laser with a 65-ps pulse duration to heat the soot and a streak camera with an 8-ps time resolution to record the signal. As with nanosecond excitation, LII signals increase during the laser pulse as soot temperatures increase and decay after the laser pulse. Signal decay rates increase significantly with increasing fluence. These short pulses may, however, be more efficient at exciting LIF from PAH at 532 nm than nanosecond pulses, leading to unexpected interferences.

Interest was also expressed in the effects that a long, microsecond, temporal profile would provide. In all cases, the temporal profile should be measured with a high-speed detector and reported.

**3.4.2 Spatial profile.** As indicated in Sect. 3.2, the spatial profile of the laser beam in the probe volume has received considerable interest. In all cases the profile is assumed uniform in the direction of the laser-beam propagation. This should be valid for most configurations, but may break down under highly attenuating circumstances such as in high-pressure heavily sooting flames [80, 106]. In the other two dimensions, numerous configurations have been employed, includ-

ing two-dimensional Gaussian, one-dimensional Gaussian sheet, near-top-hat, and full top-hat profiles.

The simplest configuration in terms of data analysis and modeling is the full top-hat profile, where all particles in the probe volume will experience the same fluence and should be heated to the same peak temperature. Examples of rectangular and circular beams with this profile are shown in Fig. 9. As illustrated, even a full top-hat profile has some variation in the spatial fluence distribution. Also, the measured profiles are time integrated over a single laser shot, and it is unknown if the spatial distribution is constant over the duration of the laser pulse. An accepted definition of what constitutes a full top-hat profile remains to be determined.

A near-top-hat profile has the bulk of the fluence at or near the maximum fluence, but there is still a substantial portion at lower fluences. Typically the edges of the profile are much more sloped than a full top-hat profile, but less so than the edges of a Gaussian beam. An illustration of the cross section of a near-top-hat profile is shown in Fig. 10 [20]. Also shown is the effect of increasing the laser fluence (energy), where the equivalent width of the laser beam is doubled as the energy is increased from 2 mJ to 15 mJ. This is due to the increasing contribution from the wings of the laser profile [107].

A one-dimensional Gaussian profile is obtained by expanding the laser beam in one direction to create a sheet with

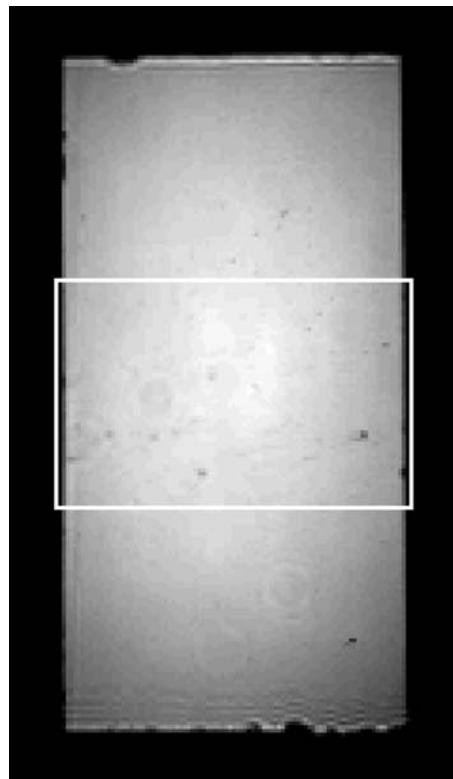


**FIGURE 9** Measured laser spatial profile of a full top-hat laser beam, for the LII system that was used to produce the sample data for evaluation (Sect. 5.1 and Table 6). The image is a 50-pulse average from a multi-mode Nd:YAG laser operating at 532 nm, passing through a  $1.5 \times 3.0 \text{ mm}^2$  aperture, and relay imaged to the detection volume with 1:1 magnification. The pixel size of the beam profiler was  $17.1 \times 19.7 \mu\text{m}^2$ . The spatial standard deviation of the intensity over the region detected by the LII receiver (indicated by the white rectangle) was 9.4%

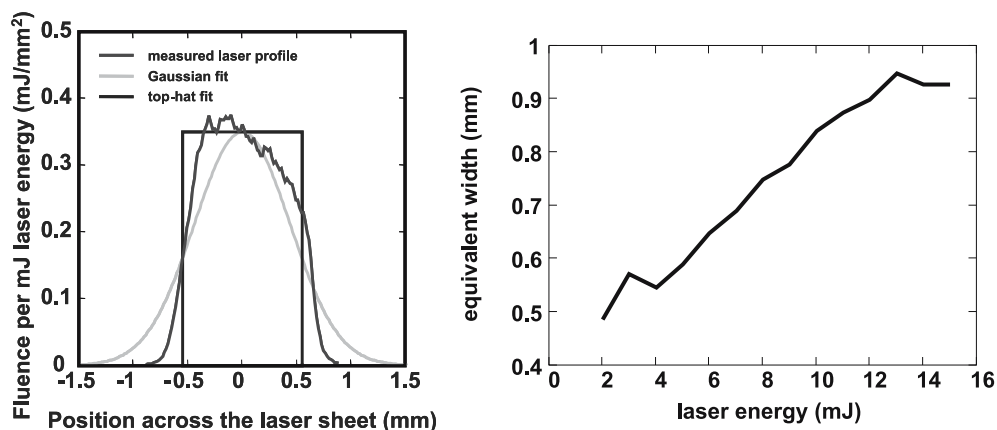


**FIGURE 10** Near-top-hat laser profile, compared to theoretical full top-hat and Gaussian profiles (*left*). The impact upon the calculated equivalent width of the near-top-hat laser profile as a function of the total laser energy (*right*) [20]

the use of a cylindrical lens, and then imaging the central region of the expanded beam, where the fluence distribution is essentially uniform in the direction of the expansion. However, the beam is still highly non-uniform in the narrow direction, resulting in large variations in temperature of the particles and in the spatial contributions to the total LII signal. As stated in Sect. 3.2, as the fluence is increased, the contributions from the wings increase, but sublimation reduces the contribution from the center of the sheet; these mechanisms offset each other under the right conditions. With this configuration, the equivalent width of the sheet is highly dependent on the laser energy, and thus the dimensions of the probe volume are highly variable, which produces large uncertainties in the spatial resolution.

The two-dimensional Gaussian profile adopted in early LII research [9, 13] has essentially been abandoned with the recognition that the particles are heated in a severely non-uniform manner. Spatial effects are well illustrated if LII is observed in a backscatter arrangement [83].

In all cases, the spatial profile should be measured with a beam profiler (CCD detector, knife edge, or pinhole) and reported along with a statement as to whether the reported fluence is the peak or the spatial average.

### 3.5 Detection strategies

The detection strategy used depends on the information one wants to derive from the measurements. For many initial applications of LII the main focus was on the determination of the distribution of soot volume fraction. Here, the laser beam is expanded with cylindrical lenses to form a sheet that illuminates a two-dimensional cross section in the measurement volume. The incandescence is detected orthogonal to the plane of the sheet with an intensified CCD camera equipped with appropriate detection filters. A large impact on the accuracy is caused by the choice of the detection gate. Since fluorescence of different species, e.g.  $C_2$  or PAH, or scattered laser light might interfere with the LII signal, delayed detection (relative to the laser pulse) was suggested in order to temporally separate the comparably long LII signal decay from interfering luminescence from short-living excited states [108, 109]. However, experimental [7, 79] and theoretical work [12] showed that long or delayed detection gates bias the LII signal towards large particles since smaller

particles cool faster than large ones (i.e. small particles have a larger surface area to volume ratio than large particles and are thus more rapidly cooled by conduction to the surrounding atmosphere). Second, conductive cooling rates increase with increasing ambient pressure and decreasing ambient temperature, leading to faster LII signal decays under these conditions [80]. If calibrations are carried out at lower pressures or higher temperatures than those under which the measurements are to be made, long or delayed detection gates should be avoided as well [37, 40]. Hence, short and prompt (i.e. with the start of the laser pulse) detection gates of 50 ns or less should be used.

In order to determine particle sizes or particle-size distributions with LII, the temporal variation in temperature or LII signal decay is used. First applications focused on the two-dimensional detection of the LII signal at two different delay times after the laser pulse in a two-camera experiment [17, 18, 110]. Because the cooling behavior of the particles depends on the primary particle size, the ratio of the images at two different delay times is related to the primary particle size (see Sect. 4.2.2 for details). For point measurements the entire LII decay curve can be used to obtain primary particle-size information from fits of numerical models to the experimental decay curve. For detection, fast photomultipliers in combination with a transient recorder, such as a digital storage oscilloscope, are used. The temporal resolution needs to be sufficient to capture the decay, which is on the order of 1  $\mu$ s in atmospheric pressure flames, but is shorter at higher pressures or lower ambient-gas temperatures. As low fluence is preferred for obtaining the primary particle diameter, the near-monotonic decay can be sampled as coarsely as in 10-ns intervals, although intervals of 1 ns or less are often used. For atmospheric pressure flame measurements the heat conduction to the surrounding gas is sufficiently slow that any significant differential cooling based on particle size will take at least tens of nanoseconds to occur, thus not requiring fast detection provided that evaporation is neglected. Most photomultipliers have rise times of 1–1.5 ns and cannot follow the rapid heating of soot. Valid experimental two-color temperature measurements during the laser pulse are very difficult to achieve. Even with a fast detector great care would be needed to temporally align the two-color signals. Small differences in detector response time or receiver spectral path lengths could make the temperatures during the laser pulse meaningless.

For a correct evaluation of the LII decay curves the peak particle temperature  $T_p^0$ , which occurs during or immediately after the laser pulse, is required as an input parameter for the model. Calculating this temperature using the absorption cross section of the soot particle and the laser fluence is associated with large uncertainty. First, the absorption cross section depends on the soot absorption function  $E(m)$ , for which the uncertainty has been discussed in Sect. 3.3. Second, in strongly absorbing environments the actual laser fluence at the measurement location is not exactly known. Instead, a two-color LII method is often used to measure the time-resolved [20] or peak [38, 93] particle temperature. It is based on the detection of the peak LII signal at two different wavelengths  $\lambda_1$  and  $\lambda_2$ . The initial signal ratio at these two wavelengths is related to the peak particle temperature based on common pyrometry [24, 111]:

$$T_p^0 = \frac{hc}{k} \left( \frac{1}{\lambda_2} - \frac{1}{\lambda_1} \right) \times \left[ \ln \left[ \frac{S_p(\lambda_1, T_p^0) K_2(\lambda_2) \varepsilon_p(\lambda_2) \lambda_1^5}{S_p(\lambda_2, T_p^0) K_1(\lambda_1) \varepsilon_p(\lambda_1) \lambda_2^5} \right] \right]^{-1} \quad (3)$$

Here,  $h$  is the Planck constant,  $c$  is the speed of light,  $k$  is the Boltzmann constant,  $S_p$  is the detected emission signal from the particles at the two detection wavelengths, and  $K_1$  and  $K_2$  are calibration constants that take into account the spectral sensitivity of the detectors at the two wavelengths. Finally,  $\varepsilon_p$  is the emissivity of the particles. The emissivity is a function of the refractive index of soot. In this case, however, the absolute value of  $E(m)$  is not required; only the ratio of  $E(m)$  at the two detection wavelengths is needed. The ratio  $\varepsilon_p(\lambda_2)/\varepsilon_p(\lambda_1)$  can be approximated by  $\lambda_1/\lambda_2$  assuming that  $E(m)$  is constant between the two wavelengths. A careful choice of the detection wavelengths is necessary. In Table 5 the detection wavelengths are listed as employed by the participants of the LII workshop. The reason for the wavelengths chosen is mainly to avoid interferences from  $C_2$  and to choose a spectral range where the detection system is most sensitive. Still, in the listed wavelengths of Table 5  $C_2$  fluorescence might interfere at 450 and 550 nm if the band pass is broad enough to collect a part of the emissions at 473 and 563 nm, respectively. A detailed overview about the choice of detection wavelengths for LII experiments is given in Sect. 3.1.

In practical situations the primary particle-size distributions and the aggregate-size distributions are both sufficiently poly-disperse that the temperature decay rate does not follow a single-exponential behavior. If the aggregates are within the RDG/PFA limit, large and small particles are heated to the same final temperature. The temperature obtained from two-color LII data is valid for all particles in the probe volume at the peak temperature only. For some researchers, this is an essential assumption as in their evaluation all particles are assumed to cool down from the same temperature. Hence, the detection of the peak signal is important, which emphasizes again the need for good temporal resolution of the detection system. Other researchers acknowledge that the time-resolved temperature measured with two-color LII is an effective temperature biased by the larger primary particles [112]. Furthermore, this assumes isolated primary particles. In aggre-

gates, the shielding will affect the cooling rate depending upon the number of primary particles per aggregate. At the LII workshop, an approach to estimate the distributions of primary particle diameter and aggregate size based on the decay of the effective temperature was presented. This work of Liu et al. [112] also identified that the initial decay rate of a soot particle ensemble at the moment of the peak soot particle temperature is inversely proportional to the Sauter mean diameter  $d_{32}$  of the poly-disperse primary soot particles, the same as that found recently for isolated primary particles [45].

### 3.6 Open questions and future experiments

Certain parameters in LII are related to (large) uncertainty. Therefore, validation experiments are planned to access these values. A list of unknown parameters has been given in Sect. 2.7. Listed below are some experimental approaches that were suggested at the LII workshop as possible experiments.

For the question about which carbon fragments evaporate from the particle surface at high laser fluences, experiments are planned to vaporize soot or graphite and detect the evaporating species with mass spectrometry. Alternatively, pump-probe experiments are planned in which a first laser pulse heats the particles at high fluences (pump) followed by a second probe pulse that resonantly excites  $C_3$  (LIF of  $C_3$ ).

The thermal accommodation might be determined in shock-tube experiments where conditions, such as bath gas temperature and bath gas composition, can be controlled. A second approach is the investigation of photolytically generated soot of the decomposition of carbon suboxide ( $C_3O_2$ ) [113]. This results in very clean carbon particles without the influence of hydrogen atoms like in flame-generated soot from hydrocarbon fuels. Different bath gases can be added to the carbon suboxide to investigate the influence of different molecular colliders and compare time-resolved LII results with transmission electron microscopy.

## 4 LII-signal evaluation

The evaluation of measured LII signals strongly depends on the underlying models. Thus, uncertainties in the models directly affect the results. This section focuses on identifying the best approaches to evaluating LII signals based on the present models. Where appropriate, the discussion differentiates between pointwise (0D) and imaging (2D) LII applications.

Section 4.1 focuses on the determination of soot volume fraction, which was the goal of LII measurements in the first applications to sooting combustion processes. Despite much progress in this field, especially regarding the handling of self-absorption [9, 81, 114, 115], there are still a number of questions that affect practical applications; these open issues are mainly related to signal calibration. In many cases a pragmatic approach is taken. This approach relies on calibration of the measurement under – at best – similar conditions.

Section 4.2 discusses effects that are connected to the determination of primary particle sizes and size distributions, which is the focus of many recent LII applications. These

LII group	Detection wavelength	Rationale	Two-color	Remarks
Bengtsson et al. Sweden, Lund	> 450 nm (short-pass filter)	Suppress flame radiation	No	
Boiarciuc et al. France, Orléans	405 and 650 nm (FWHM: 10 nm) or 441 nm (FWHM: 10 nm) and 650 nm (FWHM: 50 nm)	– Avoid C <sub>2</sub> LIF – Good spectral response PMTs or – Maximize signal for engine application	Yes	Two-color results 200–300 K below the temperature predicted by the model
Charwath et al. Germany, Karlsruhe	450 and 650 nm (FWHM: 40 ns)	No interaction with excitation wavelength	Yes	
Defuliis et al. Italy, Milano	450 and 600 nm	Best compromise – PMT sensitivity – Comparison to lamp – Sensitivity to temperature – S/N ratio	Yes	– Issue of chromaticity with lens – Delicate calibration with a lamp – Limit of the PMT range
Desgroux et al. France, Lille	> 550 nm (PMT) everything but 532 nm (ICCD)	Avoid C <sub>2</sub>	No	
Dreier et al. Switzerland, Baden	460 and 650 nm	Low spectral interference from C <sub>2</sub>	Yes (peak)	
Geigle et al. Germany, Stuttgart	TR-LII: 400 and 700 nm 2D LII: 450 nm	Wavelength difference large enough for <i>T</i> measurement Compromise between flame luminosity and signal intensity	Yes	Below 400 nm UV optics needed and strongly decreasing signal No short-pass filter Single $\lambda_{\text{det}}$ means easier signal trapping correction
Kock et al. Germany, Duisburg	550 nm and 694 nm	Maximize sensitivity of the system (PMT sensitivity + Planck law)	Yes	Issue with calibration for two-color measurements Issue with interferences at high energy at 550 nm
Nathan et al. Australia, Adelaide	415 nm	– Good S/N – No PAH signal	No	
Smallwood et al. Canada, Ottawa	397 nm (FWHM: 38 nm) and 783 nm (FWHM: 11 nm) and 532 nm (scattering)	Maximize <i>T</i> accuracy considering spectral response of PMTs, avoid interferences	Yes	Designed to minimize noise and maximize precision
Wendler et al. Germany, Erlangen	390 nm and 450 nm	Avoid fluorescence	Yes	Short-pass filter

**TABLE 5** Detection wavelength selected by LII research groups and rationale

evaluations depend critically on a fundamental understanding of the heat-loss mechanisms of the laser-heated particles. Problems in particle sizing with LII that are due to the modeling of sublimation are often circumvented by low-fluence excitation. The determination of primary particle sizes, however, is influenced by aggregate size and structure, which in turn influences the conductive heat transfer. This aspect was ignored until recently, despite research identifying these influences being published several years ago [116, 117].

#### 4.1 Determination of the soot volume fraction

Most of the earlier approaches to LII were devoted to the imaging of the spatial distribution of soot volume fraction in combustion systems. In these cases, laser fluences above the sublimation threshold were typically employed, and the correlation between the LII signal and the particle volume fraction was obtained following Melton's analysis [28]. Based on a simplified power balance for the moment of maximum particle temperature, where the radiative flux absorbed

by a particle essentially equals the heat flux by sublimation, Melton's approach yielded

$$S_{\text{LII}} \propto N_p d_p^{3+154 \text{ nm}/\lambda_{\text{det}}} . \quad (4)$$

This result indicates that the LII signal  $S_{\text{LII}}$  is related to the number  $N_p$  of primary particles in the sample volume, their size  $d_p$ , and the detection wavelength  $\lambda_{\text{det}}$ . It relies on the high-fluence limit and the approximation that the particles are small compared to the excitation wavelength. In practical cases the signal results from integration over a particle-size distribution and the spectral width of the detection system. This solution suggests that there is no linear proportionality between the LII signal and the soot volume fraction  $N_p d_p^3$ . The numerical value in the exponent of (4), however, must be treated with caution, as it relies on various model-dependent parameters that enter into the simplified power balance. Yet, although several deficiencies in Melton's model have been identified (see e.g. [34]), the major uncertainty in this value probably results from the vapor pressure of carbon, usually calculated by

the Clausius–Clapeyron equation, and thus from the heat of sublimation connected with the formation of various carbon clusters in the gas phase. While there is considerable uncertainty about the composition of the gas phase regarding these species, their enthalpies of formation are of the same order of magnitude [39]. Although there were early hints [118] to the necessity to further analyze the relation between the LII signal and the soot volume fraction, a detailed and more recent theoretical treatment is still lacking. These considerations indicate that possible deviations from a linear proportionality should be taken into account. As a consequence, even when calibrating the LII signal by an independent technique at one location, this calibration constant may change at other locations because of the evolution of primary particle sizes. For illustration of the possible influence of these effects we preliminarily employ Melton's value, assume a typical detection wavelength of 450 nm, which results in an exponent of 3.34, and consider the (rather extreme) example that a calibration at low height above burner (HAB) is applied to an LII measurement at large HAB. For a mono-disperse primary particle size of 10 nm at low HAB an evaluation based on the exponent given rather than on 3.0 would result in a calibration constant that differs by a factor of 2.2. If the particle size did not change over HAB, this deviation would not matter; if, however, the assumed size changes to 40 nm, this factor increases to a value of 3.5. This might cause an error as high as 60% in the determination of the soot volume fraction. For poly-disperse size distributions this effect is even worse because of an increasing width of the size distribution in the course of soot formation. Typically, calibration is performed at intermediate locations, and in this instance the deviation is smaller, but in the end a considerable error may result: generally, this effect might be accounted for by considering the primary particle size distribution at the respective location, which, of course, requires the knowledge of that information. To our knowledge, no experiments have been published so far attempting to incorporate primary particle sizes for correction of the calibration of volume fraction measurements. The problem of deviating particle sizes is also important when well-characterized calibration flames are employed for calibration of LII measurements in systems with spatial or temporal variability, e.g. turbulent flames [119]. In order to minimize additional size-dependent effects due to different cooling rates, it is also important to choose a temporal detection gate as short as possible and to start detection with or immediately after the laser pulse (e.g. [7, 79]).

Each calibration procedure is additionally affected by the potential (spatial or temporal) deviation of the optical properties of soot between the calibration point and the volume under investigation (see e.g. [25]). These problems are especially important when calibrating measurements in objects with large temporal or spatial variation of the soot characteristics (particle size and optical properties), e.g. turbulent flames [119] or internal combustion engines.

The calibration typically relies on an independent measurement of the soot volume fraction with an alternative technique in the same object. In most cases, laser attenuation is used. A traditional technique for determining the soot concentration is illustrated in Fig. 11. The spatially resolved LII signal as well as elastically scattered laser light is detected

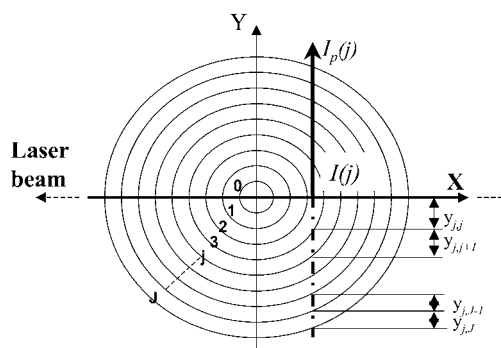


FIGURE 11 Traditional technique for correction of absorption of LII by the flame [114]. In a cylindrical flame the absorption in  $x$  and  $y$  directions is the same. If the absorption is measured in the  $x$  direction (derived from the decrease in intensity of the laser-scattered light), the absorption in the  $y$  direction of the LII signal can be corrected for

perpendicular to the direction of the laser sheet. From the attenuation of the laser sheet (derived from the decrease in the intensity of the scattering signal through the symmetric flame) the soot volume fraction can be calculated as a function of the location in the flame along the axis of the laser sheet. It should be kept in mind that the absorption is wavelength dependent and therefore different for laser and LII signals. From the observed signal distribution the soot volume fraction can be calculated in the case of steady axi-symmetric flames as a function of the location in the flame along the axis of the laser sheet.

Despite all the problems described above, several studies demonstrated a generally good agreement between soot volume fractions determined by LII and various extinction techniques, e.g. [5, 13, 19, 60]. Yet, for reasons discussed above, a universal calibration method, which is also able to deliver exact values of soot volume fractions in a 2D approach, is still lacking.

A calibration method proposed by Smallwood et al. [20, 97] relies on calibration of the LII system with a source of known radiance or irradiance. It does not require a correlation to other techniques such as extinction. The method relates the absolute intensity of the LII signal to the soot particle temperature and volume fraction. By measuring the temperature of the laser-heated soot particles with two-color pyrometry, the absolute soot volume fraction can be obtained from the absolute LII-signal intensity. For a mono-disperse particle-size distribution, it was shown that the soot volume fraction is given by

$$f_v = \frac{V_{\text{EXP}}(\lambda_{\text{em}}) \lambda_{\text{em}}^6 \left( e^{\frac{hc}{\lambda_{\text{em}} k T}} - 1 \right)}{\eta(\lambda_{\text{em}}) w_b 12\pi h c^2 E(m)}, \quad (5)$$

where  $V_{\text{EXP}}$  is the detection volume,  $\lambda_{\text{em}}$  the detection wavelength,  $w_b$  the equivalent width of the laser sheet,  $T$  the temperature,  $c$  the speed of light,  $h$  Planck's constant,  $k$  Boltzmann's constant,  $E(m)$  the soot absorption function at the detection wavelength, and  $\eta(\lambda_{\text{em}})$  a calibration constant, which is dependent on the sensitivity of the detection system. This calibration constant is determined by relating the response of the LII detection system to illumination from a traceable source. Use of this absolute intensity calibration technique for two-color LII coupled with low-fluence excitation is known

as auto-compensating LII. It accounts for variation in particle temperature due to varying experimental conditions (ambient-gas temperature, proportion of condensed organic species, laser fluence fluctuations, etc.).

## 4.2 Particle-sizing measurements

Information about mean primary particle sizes or size distributions from LII is derived from measured LII signal decay rates. At low fluences signal decay rates depend primarily on conductive cooling rates. At higher fluences changes in particle size by sublimation can contribute significantly to signal decay rates just after the laser pulse. Much of the recent work on particle sizing by these measurements has thus focused on the low-fluence regime. The evaluation of decay rates to infer particle sizes relies heavily on models of LII signal evolution. Modeled signal decay rates at low fluences strongly depend on the representation of the conductive cooling mechanism, as discussed in Sect. 2.4. The large spread in modeled decay rates shown in Figs. 1 and 2 for well-defined conditions indicates significant uncertainties in the derivation of primary particle sizes. In addition, particle shape and aggregation effects may influence a straightforward determination of primary particle sizes by LII.

*4.2.1 Temporal response of laser and detection system: point-wise measurements.* The determination of particle size depends on the evaluation of the shape of the signal decay curve and is therefore very sensitive to small distortion in the measured temporal signal decay caused by a limited temporal resolution of the experiment. The data evaluation, therefore, critically depends on an exact knowledge of the characteristics of the diagnostics system. A limited temporal resolution becomes especially important in the case of fast LII decay, e.g. for small particles, high pressures, and low ambient-gas-phase temperatures. Typically, a combination of a photomultiplier tube and a digital storage oscilloscope is used for the time-resolved detection of LII signals. The fastest standard photomultipliers have a rise time (from 10% to 90% of the maximum signal level) of 1.5 ns, which is comparable to the analog bandwidth of the input amplifier of a standard digital oscilloscope (500 MHz, 2 ns). The latter quantity is usually the limiting factor for the time resolution of a digital oscilloscope rather than the sampling rate. Even though the duration of the laser pulse (FWHM 10 ns for a Nd:YAG laser) is much longer than the time scales just mentioned, the response time of the detection system is still important. The thermal radiation of the particles depends strongly on temperature (Sect. 3.2) and, therefore, the resulting temporal gradients of the LII signal can be much steeper than one would expect from the temporal evolution of the laser pulse.

The influence of an insufficient temporal resolution of the detection system is most pronounced at highest signal gradients, which appear during the heat-up phase shortly before reaching peak temperature. As a consequence, the maximum of the observed LII-signal intensity is decreased, delayed, and broadened compared to the actual emission intensity that would be detected with unlimited temporal resolution. Details of the consequences of insufficient temporal resolution of the detection system are discussed in a separate article in

this issue [120]. Nevertheless, if a detection system with an insufficient time resolution is used, particle sizes and size distributions may be derived correctly after calibration, based on the assumption of incorrect values for the underlying constants (e.g. the thermal accommodation coefficient). In this case, the universal validity of these constants for different flame conditions would be restricted.

These effects have been discussed in the research work performed by Bougie et al., who measured time-resolved LII in a heavy-duty diesel engine with peak pressures up to 6 MPa [121, 122]. Being aware that at this pressure the decay of the measured LII signal is influenced by the laser/detector response time, the particle size was obtained by deconvoluting the LII signal and the response function of the system. Especially for small particles, at even higher pressures and/or lower ambient-gas temperatures the decay of the LII signal tends to approximately follow the temporal shape of the laser pulse. In this case, short-pulse lasers and fast detection systems should possibly be applied in order to obtain information about the particle-size distribution from the temporal evolution of the LII signal (see e.g. [105]).

*4.2.2 Two-dimensional determination of particle sizes.* For two-dimensional determination of particle sizes by time-resolved LII, the time response of the detection system is further decreased. Typically, two images are taken subsequently that time-integrate signals from different parts in the cooling curve. In this case, the choice of suitable detection intervals is important. While for the first observation interval usually a prompt or near-prompt gate is employed, (a delay by some tens of nanoseconds may be favorable to avoid fluorescence interference), the choice of the second gate is a more complex problem where a compromise between sensitivity to particle size (i.e. late second detection interval) and signal-to-noise statistics (i.e. early interval with strong signal) must be achieved. This choice strongly depends on the noise characteristics of the experiment. Such an analysis was performed by Will et al. [17] for an LII application in an atmospheric pressure flame, where a fair agreement between the underlying statistical model and experimental data was found and which resulted in the suggested use of the second detection interval of about 600–800 ns after the laser pulse. In most applications today, earlier second intervals are used. Especially in high-pressure environments, where the decay rate of the time-resolved LII signals is much higher, the second gate should be chosen at a much shorter delay. All these choices often seem somewhat arbitrary, however, and it might be worthwhile to pay more attention to this issue again in imaging particle-size LII applications.

*4.2.3 Determination of particle-size distributions.* Retrieving a particle-size distribution from a given LII signal or particle-temperature decay is an ill-posed problem. Coarsely different particle-size distributions may result in very similar signals rendering a proper inversion difficult. This problem finds its mathematical origin in the fact that a superposition of different exponentially decaying functions is close to a simple exponential decay. As the analysis of such exponential-like decays is a problem frequently encountered in natural

sciences, there exist a number of approaches that may be similarly applied to time-resolved LII. An initial approach by Roth and Filippov [30] uses a standard inversion scheme for the solution of first-kind Fredholm integral equations without relying on assumptions about a specific shape of the distribution. In order to reduce ambiguity, later approaches usually assumed a certain type of distribution function (typically log-normal). Lehre et al. [38] proposed a direct non-linear regression, i.e. minimizing the deviation between the experimental signal and test functions parameterized by a median value and a geometrical width. They underlined the necessity to employ their fits over long time intervals in order to avoid ambiguous results [22]. This approach, therefore, required a detection scheme with high dynamic range and efficient signal collection.

Driven by the desire to avoid iterative evaluation procedures for on-line applications, direct approaches were proposed for the determination of particle-size distributions. Here, the parameters from a quick fit were related to the moments of the particle-size distribution. Possible schemes used a fit to two different time intervals [123] or a cumulant approach [124], where the signal function is approximated by an expression of the form

$$S \propto \exp\left(-K_1 t + \frac{K_2}{2} t^2\right). \quad (6)$$

All approaches basically try to find characteristic deviations from a simple exponential decay. In the presence of experimental noise it is therefore often difficult to find the correct solution. Furthermore, because of the nature of the ill-posed problem, the resulting parameters median diameter and distribution width are highly interdependent. In a somewhat intermediate approach between a fully iterative procedure for error minimization and a direct two-parameter fit, Liu et al. [45] recently proposed inferring a Sauter mean diameter from the initial temperature decay. The width of the distribution is then determined from an iteration that yields a best match between calculated particle temperatures of theoretical test distributions and the particle temperature determined by two-color LII at late times (in a flame case at about 1.5  $\mu$ s).

**4.2.4 Detection of small particles in the presence of large ones.** In poly-disperse particle samples the observable meas-

ured temporal evolution of the LII emission is a combination of the size-dependent LII decay of the different particle-size classes. The small volume fraction of the smallest particles within a particle-size distribution severely restricts their contribution to the total LII signal. The overall time dependence of the signal will therefore predominantly reflect the characteristics of the large particles. In order to distinguish between particles that significantly contribute to the overall signal and those that do not, a ‘threshold radius’ has been defined [125]. All particles below this radius contribute to less than 10% of the signal intensity at a given time (at  $\lambda_{\text{det}} = 450$  nm). Because of the faster cooling of the small particles, their signal contribution decreases at longer delay times resulting in increasing threshold radii with time.

This effect is illustrated in Fig. 12, in which the threshold radii (Fig. 12b) are plotted as a function of time for exemplary particle-size distributions depicted in the left-hand figure in Fig. 12. This effect has been investigated for an equal size distribution in the 1–25 nm range, for two log-normal size distributions with  $r_m = 5$  nm and  $r_m = 20$  nm (both with  $\sigma = 0.34$ ) and for a bimodal distribution, which is given by the arithmetic average of both log-normal distributions. At  $t = 0$  ns all particles have the same temperature. With increasing time the temperature of the particles becomes size dependent. Smaller particles cool down to lower temperatures compared to large ones. Therefore, the contribution of the small particles to the overall LII signal decreases over time, and the remaining LII signal becomes increasingly weighted towards the larger particles. As shown in Fig. 12b, the threshold radius is 14 nm for the equal distribution  $1 \text{ nm} < r < 25 \text{ nm}$  at  $t = 0$  ns. Therefore,  $(14 - 1)/(25 - 1) = 54\%$  of the particles represent only 10% of the soot volume fraction. In other words, more than half of the particles do not contribute significantly to the total LII signal. This effect is even more pronounced for a log-normal size distribution. The insensitivity of the temporal evolution of the LII signal to smaller particles is further illustrated by the investigation of a bimodal distribution. Even though the relative number of small particles of the bimodal distribution is much higher compared to the log-normal size distribution with  $r_m = 20$  nm, the temporal evolution of the threshold radius for both distributions is more or less identical. Only during the first  $\sim 200$  ns can small differences be observed. These evaluations show that one cannot deduce the

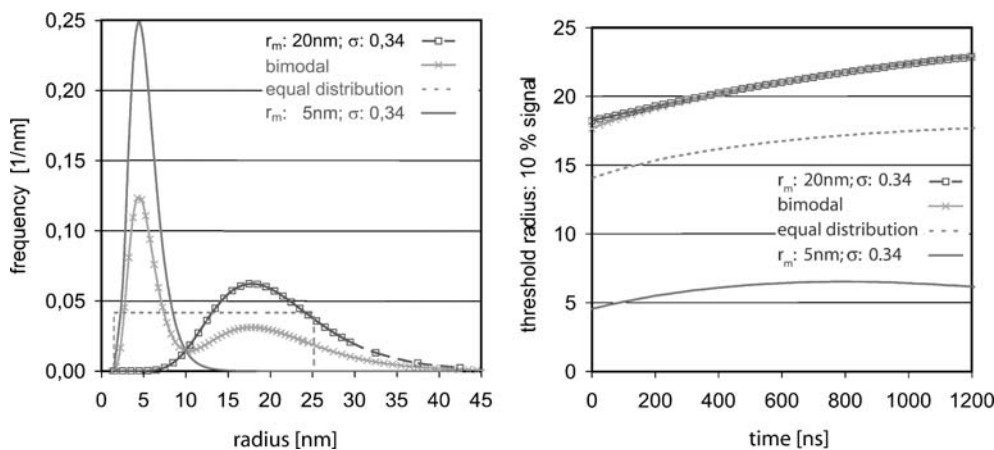


**FIGURE 12** Threshold radius (right-hand figure) for different size distributions (left-hand figure) [125]

particle number concentration of a large fraction of all particles within a particle-size distribution. Therefore, without a priori assumptions about the shape of the distribution, no conclusions are possible concerning the complete particle-size distribution and, hence, about the number density of small particles. However, based on the assumption of the shape of the particle-size distribution (e.g. log-normal), results can also be obtained for the number of smaller particles within the particle-size distribution as well.

**4.2.5 Influence of particle shape and aggregation.** Originally, all LII models were based on the idealized assumption of spherical particles that are not affected by the real aggregate structure. Under these conditions the specific surface as determined from the signal decay is directly linked to the diameter of these particles.

TEM recordings from soot particles formed in laminar pre-mixed flat low-pressure flames showed, however, that at increasing heights above the burner the particle shape can change from spheres to rotational ellipsoids caused by coagulation processes and surface-growth reactions [126]. Rotational ellipsoids have larger surface-to-volume ratios than spheres, which lead to increased sublimation and heat conduction. This difference could lead to differences in the temporal evolution of the LII signal [21]. In addition, TEM images have demonstrated that even nominally spherical primary particles can form aggregates coated with layers of carbon, which have a significantly reduced specific surface area (area per unit volume) compared to aggregates of spherical primary particles connected by point contact [127]. These deviations from idealized behavior result in a reduced heat-exchanging surface and thus in an overestimation of expected signal decay rates for a particular particle size, leading to an overestimation of particle diameters, unless this effect is implicitly accounted for in a corresponding choice of the thermal accommodation coefficient.

Apart from this direct influence of the cluster structure of soot on the free particle surface, there is an additional effect, namely the reduction of conductive particle cooling due to the aggregate structure, which conventionally has not explicitly been considered in the LII literature. After the initial treatment by Filippov et al. [116, 117] this problem was recently investigated by Snelling et al. [41] and Liu et al. [46, 112] who demonstrated, based on different heat-conduction models, that this shielding effect may reduce the heat flux for conductive cooling by an order of several tens of percent for typical soot structures. Although this effect is partially accounted for in the choice of a ‘mean’ thermal accommodation coefficient, for an accurate evaluation of LII the number of parameters that need to be included in the data evaluation is continuously increasing. Consequently, the LII evaluation must aim not only at the determination of primary particle-size distributions, but additionally at those of aggregate size. Future trends should be directed towards the inclusion of aggregate-size distribution or – even further – aggregate structure into the evaluation.

**4.2.6 Gas-phase temperature.** The local gas-phase temperature must be known to a high degree of accuracy, as this quantity – together with the thermal accommodation coefficient

– is one of the key parameters that directly influence the result of the evaluation. If the local gas-phase temperature  $T_{\text{gas}}$  is unknown, the particle-size distribution can still be estimated if a two-color-LII technique [38, 93] is applied and the following assumptions are made:

- Before the heat-up of the particles by the laser pulse, the particles are in thermodynamic equilibrium with the surrounding gas phase, e.g. the temperature of the particle  $T_0$  is identical to the gas-phase temperature  $T_{\text{gas}}$ .
- The particles are heated up very rapidly compared to the time scale of the cooling mechanisms.

Especially for low laser fluences the latter assumption is reasonable, because the heat-up rates are more than one order of magnitude faster than the cooling rates. Neglecting the cooling mechanisms to the surrounding gas phase during the heat-up phase of the particle simplifies the energy-balance equation to two terms: the absorptive heating rate  $A$  and the rise of the internal energy  $I$ . In this case  $A = I \sim T_{\text{max}} - T_{\text{gas}}$ , and the maximum temperature  $T_{\text{max}}$  of the particles depends on the initial particle or gas-phase temperature. If  $T_{\text{max}}$  is measured by a two-color-LII technique, the particle-size distribution can be estimated.

**4.2.7 Combination of LII with further measurement techniques.** As detailed above, the inclusion of aggregate size and structure has evolved as a critical point for the accurate determination of primary particle size via LII. Favorably, various scattering/extinction methods are employed additionally to LII as they also allow for an in situ determination of the quantities required. Excellent reviews in this field were given by Jones [128] and Sorensen [129]. Apparently, one problem in this context is to correctly account for the real structure of soot aggregates, which may significantly differ from the idealized model of spheres with point contact. This problem calls for the application of more complex scattering theories, like the  $T$ -matrix method [130], the finite-difference time-domain scheme [131], or the discrete dipole approximation [132]. Despite the immense computational time required, it is not clear to what extent these approaches can reveal information about the true aggregate structure. A limitation of most scattering methods is that, apart from the theoretical and experimental effort required, they usually provide pointwise information only. In this context, it is worthwhile to again consider an intensified use of a combination of LII and elastic scattering. Although the depth of information is limited in comparison to sophisticated scattering/extinction methods, this combination offers the advantage of simultaneous access to full 2D information on aggregate sizes. The basic concept is to replace the information obtained from extinction by an equivalent LII contribution. A first successful approach to obtain relative aggregate sizes in this way was performed by Will et al. [18, 110], but it relied on a simplified structure factor and did not yield absolute values as no calibration was performed. The combination of LII and elastic scattering was also employed by a number of other researchers, e.g. in the RAYLIX approach by Bockhorn and Suntz [109]. This research, however, did not aim at the determination of aggregate sizes, and thus further work on the 2D determination of this important quantity is desirable.

## 5 Comparison of sample data evaluation and target flame measurements

### 5.1 Sample data evaluation

For a further comparison of the different models used for LII-signal analysis, three sample data sets of time-resolved LII measurements were provided to all participants of the LII workshop 2005. The experimental data were obtained by NRC with an auto-compensating LII experimental system and laminar diffusion flames, described in [20], for the following cases:

- Condition A:  
Mid-level fluence experiment at  $0.50 \text{ mJ/mm}^2$ .  $T_g = 1750 \text{ K}$ .
- Condition B:  
Higher-level fluence experiment at  $0.75 \text{ mJ/mm}^2$ .  $T_g = 1750 \text{ K}$ .
- Condition C:  
Mid-level fluence experiment at  $0.8 \text{ mJ/mm}^2$ .  $T_g = 575 \text{ K}$ .

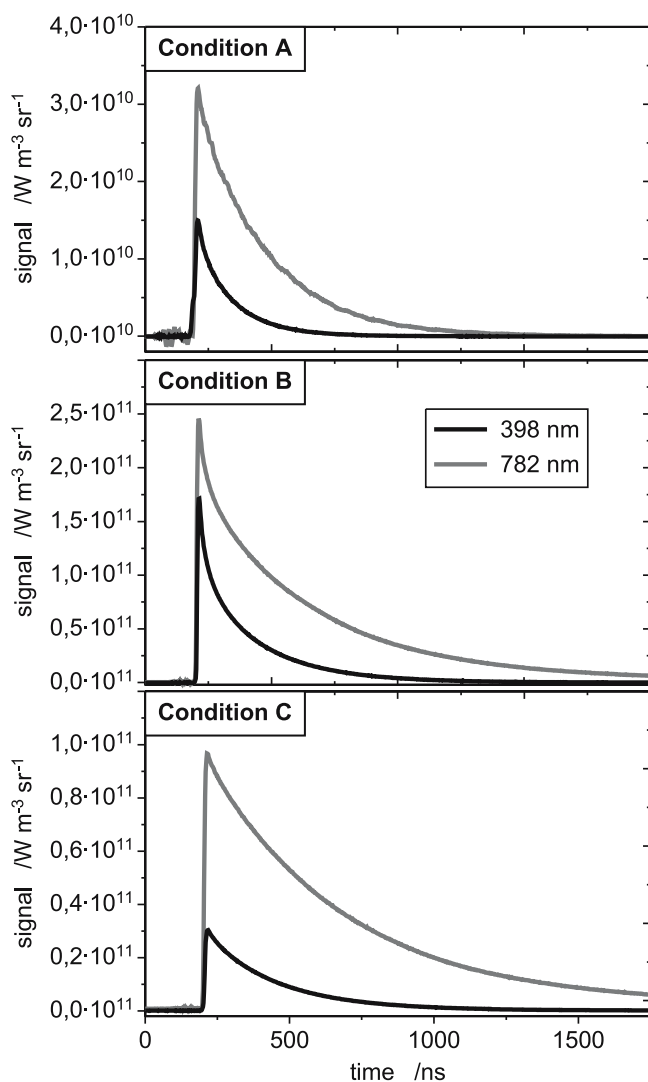


FIGURE 13 Sample data signals for the conditions A, B, and C under the consideration of the sensitivity of the detection system. These data are the input for the data evaluation performed by three different research groups. The results are compiled in Table 6

The gas pressure was  $p_g = 1 \text{ bar}$  for all experiments. Additionally, the temporal and spatial laser profile and the calibration factors for the two-color experiments were made available. The excitation wavelength for all provided data sets was  $532 \text{ nm}$ , generated with a frequency-doubled (non-seeded) Nd:YAG laser. The response time of the LII-signal photomultipliers is  $1.8 \text{ ns}$ . The presented data (Fig. 13) originates from multi-pulse averages with a temporal jitter below  $1 \text{ ns}$ . Each data set provided two time-dependent signal traces detected at  $398 \text{ nm}$  and  $782 \text{ nm}$ , respectively. The detection filter function for the applied multi-cavity interference filters can be reasonably approximated with a square profile.

The three signal traces were evaluated based on the models of Liu et al. [45], Bockhorn [38], and Kock–Roth [43, 53], all assuming that the primary particle diameter distribution is log-normal, i.e.

$$f(d_p) = \frac{1}{\sqrt{2\pi}d_p \ln \sigma_g} \exp \left[ -\frac{(\ln d_p - \ln d_g)^2}{2(\ln \sigma_g)^2} \right].$$

The resulting values of the particle heat-up temperatures  $T_p^0$ , the geometric mean diameter  $d_g$ , and the geometric standard deviation  $\sigma_g$  are summarized in Table 6. For the Kock–Roth model the particle heat-up temperatures were determined both by a calculation based on absorption theory (refractive index according to [54]) and by two-color pyrometry, respectively.

In the case of condition C, Liu et al. found that the peak particle temperature is significantly underpredicted by using the same model parameters as for condition A with  $T_g = 575 \text{ K}$ . In order to reproduce the experimental peak particle temperature of about  $3690 \text{ K}$ , the gas temperature was increased to  $1000 \text{ K}$ .

### 5.2 Target flame measurements

During the preparation for the LII workshop 2005 three target flames were defined for measurements in different laboratories under identical conditions. Burner configurations were chosen that are widespread in the combustion community. The conditions for sooting flames in a modified McKenna burner [16], a Gülder burner [133], and a Santoro burner [13] are given in Table 7, and photographs of the resulting flames are shown in Fig. 14.

The stabilized McKenna flame that was previously used in [16] has the lowest soot volume fraction and is therefore best suited for additional gas-phase measurements. The sta-



FIGURE 14 Target flames: modified McKenna (left), Gülder (center), Santoro (right). Operating conditions and measurement positions are given in Table 7

		Liu et al.	Charwith– Bockhorn	Kock–Roth			
				Single-color method 398 nm	782 nm	Two-color method 398 nm 782 nm	
Condition A	$T_p^0$	3400 K	3370 K	2880 K		3405 K	
	$d_g$	36 nm	36 nm	22 nm	23 nm	32 nm	30 nm
	$\sigma_g$	1.29	1.13	1.14	1.10	1.10	1.10
Condition B	$T_p^0$	*	3900 K	3445 K		4026 K	
	$d_g$	*	**	17 nm	23 nm	102 nm	55 nm
	$\sigma_g$	*	**	1.42	1.16	1.10	1.10
Condition C	$T_p^0$	3690 K	2450 K	2383 K		3702 K	
	$d_g$	37 nm ***	48 nm	36 nm	29 nm	55 nm	47 nm
	$\sigma_g$	1.42 ***	1.46	1.20	1.45	1.10	1.10

\* The method of Liu cannot be applied to high fluence. Case B was not analyzed

\*\* No solution fits the experimental temperature decay for the given conditions

\*\*\* The gas temperature was changed to 1000 K

**TABLE 6** Results of the sample data analysis (cf. Fig. 13) for particle heat-up temperatures  $T_p^0$ , geometric mean diameter  $d_g$ , and the geometric standard deviation  $\sigma_g$

Burner type	McKenna burner with stabilization plate**	Gülder burner	Santoro burner
Fuel	Ethylene/air	Ethylene/air	Ethylene/air
Fuel/air equi- valence ratio $\varphi$	2.1	Non-pre-mixed	Non-pre-mixed
Flow rate	10 slm (fuel/air mixture)	0.194 slm ethylene	0.231 slm ethylene
Coflow	No	284 slm air	43 slm air
Measurement position	12 mm above burner centerline	42 mm above burner centerline	50 mm above burner centerline
Comments	Measurement $\sim$ 15 min after ignition	Visible flame height $\sim$ 65 mm	Chimney ( $\sim$ 200-mm dia.) to stabilize the flame

**TABLE 7** Target flames and measurement conditions. McKenna burner modified by a flat stainless-steel stabilization plate (diameter 60 mm, thickness 20 mm) at 21 mm above the burner

Burner type	McKenna burner with stabilization plate*	Gülder burner	Santoro burner
Soot volume fraction (LII)	DLR: $\sim$ 0.03 ppm LTH: $\sim$ 0.09 ppm	NRC: $3.9 \pm 0.1$ ppm CIENI: 4.5–5.0 ppm	Yale: 3 ppm IVG: 3.7 ppm
Soot volume fraction (absorption)	–	NRC: 4.0 ppm	Santoro et al. [134]: 4.3 ppm
Soot volume fraction (other methods)	CIENI: 5.0 ppm IVG: 4.5 ppm	–	Köylü et al. [135] (TSPD): 3.8 ppm McEnally et al. [136] (TPD): 5.5 ppm
Soot primary particle size (LII)	DLR: 11.9 nm LTH: 12 nm IVG: 16.8 nm, $\sigma = 1.1$	NRC: 29 nm IVG: 32 nm ( $\alpha = 0.23$ )	IVG: 74 nm, $\sigma = 1.5$
Soot primary particle size (TEM)	IVG: 17.4 nm, $\sigma = 1.13$	NRC: 29.3 nm IVG: 29.6 nm, $\sigma = 1.21$	IVG: 29.3 nm, $\sigma = 1.18$ Dobbins and Megaridis [137]: $35 \pm 3$ nm Köylü et al. [135]: 31 nm Vander Wal et al. [138]: $33.3 \pm 3.2$ nm Puri et al. [139]: 32 nm
Gas-phase temperature	Lund (CARS): 1715 K IVG (NO-LIF): 1560 K	NRC (CARS) $1725 \pm 25$ K	Santoro and Miller [140] (TC): 1600 K Vander Wal et al. [138] (TC): 1600 K Dobbins et al. [141] (TC): 1584 K Köylü et al. [135] (TC): 1600 K
Particle temperature (soot pyrometry)	–	NRC: $1640 \pm 60$ K	–
Particle carbon- to hydrogen-atom ratio	–	–	Dobbins et al. [141]: 5.94

**TABLE 8** Experimental results in the target flames. Contributing groups: CIENI (S. Deluiliis, University Milan), DLR (K.P. Geigle, DLR-Stuttgart), IVG (B. Tribalet, B. Kock, C. Schulz, Universität Duisburg-Essen), LTH (P.-E. Bengtsson, Lund University), NRC (G. Smallwood, National Research Council Canada), Sandia (H. Michelsen, CRF Sandia, Livermore, CA), and Yale (B. Connelly, M. Long, Yale University)

bilization plate, however, introduces a temporal variation of the flame during heat-up. Therefore, measurements have been carried out at a fixed delay of  $\sim 15$  min after ignition. The Gülder burner generates a stable strongly sooting flame that is well suited as a target flame. The Santoro flame under the given flow conditions needs a chimney for stabilization. Because of potential slight variations in the chimney arrangement and geometry, the reproducibility of this setup in different laboratories seems questionable. All three flames will be continuously used by the LII community as target flames. The aim is to improve the knowledge about these flames to provide standardized flame conditions that can be used for validation and calibration experiments. The data available to date are shown in Table 8. The data include measurements of soot volume fractions by LII and laser absorption, primary particle size by time-resolved LII and TEM sampling, and gas-phase (CARS and NO-LIF) and particle (soot pyrometry) temperatures. The results that have been contributed by the different groups show the typical uncertainty of the absolute measurements.

**ACKNOWLEDGEMENTS** The authors thank P.-E. Bengtsson and H. Bladh (LTH, Lund, Sweden), A. Boiarciuc (Université de Orléans, France), T. Dreier (PSI, Villigen, Switzerland), R. Hedef (DLR, Stuttgart, Germany), and F. Liu (NRC, Ottawa, Canada) for providing additional calculations for the comparison of LII models. S. DeLuliis (CIENI, Milan, Italy), K.-P. Geigle (DLR, Stuttgart, Germany), and B. Connelly (Yale, USA) provided experimental data for the comparison of LII measurements in the target flames. Financial support for the organization of the International Workshop on LII by Deutsche Forschungsgemeinschaft and Duisburger Universitätsgesellschaft is gratefully acknowledged.

## REFERENCES

- J.E. Dec, SAE Tech. Paper Ser. 920115 (1992)
- J.E. Dec, A.O. zur Loye, D.L. Siebers, SAE Tech. Paper Ser. 910224 (1991)
- C. Espey, J.E. Dec, SAE Tech. Paper Ser. 930971 (1993)
- N.P. Tait, D.A. Greenhalgh, Ber. Bunsenges. Phys. Chem. **97**, 1619 (1993)
- R.L. Vander Wal, K.J. Weiland, Appl. Phys. B **59**, 445 (1994)
- R.L. Vander Wal, D.L. Dietrich, Appl. Opt. **34**, 1103 (1995)
- T. Ni, J.A. Pinson, S. Gupta, R.J. Santoro, Appl. Opt. **34**, 7083 (1995)
- J.A. Pinson, D.L. Mitchell, R.J. Santoro, SAE Tech. Paper Ser. 932650 (1993)
- C.R. Shaddix, K.C. Smyth, Combust. Flame **107**, 418 (1996)
- C. Allouis, A. D'Alessio, C. Noviello, F. Beretta, Combust. Sci. Technol. **153**, 51 (2000)
- A.V. Filippov, M.W. Markus, P. Roth, J. Aerosol Sci. **30**, 71 (1999)
- B. Mewes, J.M. Seitzman, Appl. Opt. **36**, 709 (1997)
- B. Quay, T.-W. Lee, T. Ni, R.J. Santoro, Combust. Flame **97**, 384 (1994)
- P. Roth, O. Brandt, S. von Gersum, Proc. Combust. Inst. **23**, 1485 (1990)
- S. Schraml, S. Will, A. Leipertz, SAE Tech. Paper Ser. 1999-01-0146 (1999)
- B. Axelsson, R. Collin, P.-E. Bengtsson, Appl. Opt. **39**, 3683 (2000)
- S. Will, S. Schraml, K. Bader, A. Leipertz, Appl. Opt. **37**, 5647 (1998)
- S. Will, S. Schraml, A. Leipertz, Opt. Lett. **20**, 2342 (1995)
- B. Axelsson, R. Collin, P.-E. Bengtsson, Appl. Phys. B **72**, 367 (2001)
- D.R. Snelling, G.J. Smallwood, F. Liu, Ö.L. Gülder, W.D. Bachalo, Appl. Opt. **44**, 6773 (2005)
- J. Appel, B. Jungfleisch, M. Marquardt, R. Suntz, H. Bockhorn, Proc. Combust. Inst. **26**, 2387 (1996)
- H. Bockhorn, H. Geitlinger, B. Jungfleisch, T. Lehre, A. Schön, T. Streibel, R. Suntz, Phys. Chem. Chem. Phys. **4**, 3780 (2002)
- B.F. Kock, T. Eckhardt, P. Roth, Proc. Combust. Inst. **29**, 2775 (2002)
- D.R. Snelling, G.J. Smallwood, R. Sawchuk, W.S. Neill, D. Gareau, W. Chippior, F. Liu, W. Bachalo, Ö.L. Gülder, SAE Tech. Paper Ser. 2000-01-1994 (2000)
- M.S. Tsurikov, K.P. Geigle, V. Krüger, Y. Schneider-Kühnle, W. Stricker, R. Lückerrath, R. Hedef, M. Aigner, Combust. Sci. Technol. **177**, 1835 (2005)
- R.W. Weeks, W.W. Duley, J. Appl. Phys. **45**, 4661 (1973)
- A.C. Eckbreth, J. Appl. Phys. **48**, 4473 (1977)
- L.A. Melton, Appl. Opt. **23**, 2201 (1984)
- D.L. Hofeldt, SAE Tech. Paper Ser. 930079 (1993)
- P. Roth, A.V. Filippov, J. Aerosol Sci. **27**, 95 (1996)
- K.R. McManus, J.H. Frank, M.G. Allen, W.T. Rawlins, in *Proc. Am. Inst. Aeronautics and Astronautics, Vol. 36*, AIAA 98-0159 (1998)
- S. Schraml, S. Dankers, K. Bader, S. Will, A. Leipertz, Combust. Flame **120**, 439 (2000)
- D. Snelling, F. Liu, G.J. Smallwood, Ö.L. Gülder, in *Proc. 34th National Heat Transfer Conf.*, NHTC 2000-12132, Pittsburgh, PA, Aug. 20–22 (2000)
- G.J. Smallwood, D. Snelling, F. Liu, Ö.L. Gülder, J. Heat Transf. **123**, 814 (2001)
- T. Schittkowski, B. Mewes, D. Brüggemann, Phys. Chem. Chem. Phys. **4**, 2063 (2002)
- C. Allouis, F. Beretta, A. D'Alessio, Exp. Therm. Fluid Sci. **27**, 455 (2003)
- H. Bladh, P.-E. Bengtsson, Appl. Phys. B **78**, 241 (2004)
- T. Lehre, B. Jungfleisch, R. Suntz, H. Bockhorn, Appl. Opt. **42**, 2021 (2003)
- H.A. Michelsen, J. Chem. Phys. **118**, 7012 (2003)
- H.A. Michelsen, P.O. Witze, D. Kayes, S. Hochgreb, Appl. Opt. **42**, 5577 (2003)
- D.R. Snelling, F. Liu, G.J. Smallwood, Ö.L. Gülder, Combust. Flame **136**, 180 (2004)
- V. Krüger, C. Wahl, R. Hedef, K.P. Geigle, W. Stricker, M. Aigner, Meas. Sci. Technol. **16**, 1477 (2005)
- B.F. Kock, C. Schulz, P. Roth, Combust. Flame, in press (2006)
- R. Hedef, V. Krüger, K.P. Geigle, M.S. Tsurikov, Y. Schneider-Kühnle, M. Aigner, Int. Rev. Inst. Fr. Pétrole, in press (2005)
- F. Liu, B.J. Stagg, D.R. Snelling, G.J. Smallwood, Int. J. Heat Mass Transf. **49**, 777 (2006)
- F. Liu, G.J. Smallwood, D.R. Snelling, J. Quantum Spectrosc. Radiat. Transf. **93**, 301 (2005)
- W.H. Dalzell, A.F. Sarofim, J. Heat Transf. **91**, 100 (1969)
- B.J. McCoy, C.Y. Cha, Chem. Eng. Sci. **29**, 381 (1974)
- H.R. Leider, O.H. Krikorian, D.A. Young, Carbon **11**, 555 (1973)
- S.S. Krishnan, K.-C. Lin, G.M. Faeth, J. Heat Transf. **123**, 331 (2001)
- S.C. Lee, C.L. Tien, Proc. Combust. Inst. **18**, 1159 (1981)
- R. Starke, B. Kock, P. Roth, Shock Waves **12**, 351 (2003)
- B.F. Kock, C. Kayan, J. Knipping, H.R. Orthner, P. Roth, Proc. Combust. Inst. **30**, 1689 (2005)
- H. Chang, T.T. Charalampopoulos, Proc. R. Soc. London. Ser. A **430**, 577 (1990)
- A.V. Filippov, D.E. Rosner, Int. J. Heat Mass Transf. **43**, 127 (2000)
- C. Kittel, *Introduction to Solid State Physics* (Wiley, New York, 1986)
- E.A. Rohlffing, J. Chem. Phys. **89**, 6103 (1988)
- C.B. Stipe, J.H. Choi, D. Lucas, C.P. Koshland, R.F. Sawyer, J. Nanopart. Res. **6**, 467 (2004)
- P.-E. Bengtsson, M. Aldén, Appl. Phys. B **60**, 51 (1995)
- C. Schoemaeker Moreau, E. Therssen, X. Mercier, J.F. Pauwels, P. Desgroux, Appl. Phys. B **78**, 485 (2004)
- D.S. Coe, J.I. Steinfeld, Chem. Phys. Lett. **76**, 485 (1980)
- F. Ossler, T. Metz, M. Aldén, Appl. Phys. B **72**, 479 (2001)
- F. Ossler, T. Metz, M. Aldén, Appl. Phys. B **72**, 465 (2001)
- A. Leipertz, F. Ossler, M. Aldén, in *Applied Combustion Diagnostics*, ed. by K. Kohse-Höinghaus, J.B. Jeffries (Taylor and Francis, New York, 2002), pp. 359–383
- R.L. Vander Wal, Proc. Combust. Inst. **27**, 2269 (1996)
- R.L. Vander Wal, K.A. Jensen, M.Y. Choi, Combust. Flame **109**, 399 (1997)
- R.L. Vander Wal, Combust. Flame **112**, 607 (1998)
- K.C. Smyth, C.R. Shaddix, D.A. Everest, Combust. Flame **111**, 185 (1997)
- P. Andreussi, B. Barbieri, L. Petarca, Combust. Sci. Technol. **49**, 123 (1986)
- A. Gomez, M.G. Littman, I. Glassman, Combust. Flame **70**, 225 (1987)
- L. Petarca, F. Marconi, Combust. Flame **78**, 308 (1989)
- F. Cignoli, S. Benecchi, G. Zizak, Opt. Lett. **17**, 229 (1992)
- C.S. McEnally, L.D. Pfefferle, Combust. Flame **121**, 607 (2000)

- 74 A. Ciajolo, B. Apicella, R. Barbella, A. Tregrosso, F. Beretta, C. Al-louis, *Energ. Fuel* **15**, 987 (2001)
- 75 T.L. Farias, M.G. Carvalho, Ü.Ö. Köylü, G.M. Faeth, *J. Heat Transf.* **117**, 152 (1995)
- 76 T.L. Farias, Ü.Ö. Köylü, M.G. Carvalho, *Appl. Opt.* **35**, 6560 (1996)
- 77 G.W. Mulholland, R.D. Mountain, *Combust. Flame* **119**, 56 (1999)
- 78 G.W. Mulholland, C.F. Bohren, K.A. Fuller, *Langmuir* **10**, 2533 (1994)
- 79 R.L. Vander Wal, *Appl. Opt.* **35**, 6548 (1996)
- 80 M. Hofmann, W.G. Bessler, C. Schulz, H. Jander, *Appl. Opt.* **42**, 2052 (2003)
- 81 D.J. Bryce, N. Ladomatos, H. Zhao, *Appl. Opt.* **39**, 5012 (2000)
- 82 R.L. Vander Wal, K.A. Jensen, *Appl. Opt.* **37**, 1607 (1998)
- 83 H. Bladh, P.E. Bengtsson, J. Delhay, Y. Bouvier, E. Therssen, P. Desgroux, *Appl. Phys. B* (2006), DOI: 10.1007/s00340-006-2197-y
- 84 P. Monchicourt, *Phys. Rev. Lett.* **66**, 1430 (1991)
- 85 S. Arepalli, C.D. Scott, *Chem. Phys. Lett.* **302**, 139 (1999)
- 86 S. Arepalli, P. Nikolaev, W. Holmes, C.D. Scott, *Appl. Phys. A* **70**, 125 (2000)
- 87 A.A. Poretzky, D.B. Geohegan, X. Fan, S.J. Pennycook, *Appl. Phys. Lett.* **76**, 182 (2000)
- 88 R.L. Vander Wal, T.M. Tichich, A.B. Stephens, *Appl. Phys. B* **67**, 115 (1998)
- 89 W. Koehnner, *Solid-State Laser Engineering* (Springer, Berlin, 1999)
- 90 D. Choi, M. Iwamuro, Y. Shima, J. Senda, H. Fujimoto, *SAE Tech. Paper Ser.* 2001-01-1255 (2001)
- 91 A.E. Greis, G. Grünefeld, M. Becker, S. Pischinger, Quantitative measurements of the soot distribution in a realistic common rail D.I. Diesel engine. In *11th Int. Symp. Application of Laser Techniques to Fluid Mechanics*, Lisbon, 2002
- 92 T.R. Meyer, S. Roy, V.M. Belovich, E. Corporan, J.R. Gord, *Appl. Opt.* **44**, 445 (2005)
- 93 B.F. Kock, P. Roth, Two-color TR-LII applied to in-cylinder Diesel particle sizing. In *Proc. Eur. Combustion Meet.*, Orléans (2003)
- 94 G.D. Yoder, P.K. Diwakar, D.W. Hahn, *Appl. Opt.* **20**, 4211 (2005)
- 95 P.O. Witze, S. Hochgreb, D. Kayes, H.A. Michelsen, C.R. Shaddix, *Appl. Opt.* **40**, 2443 (2001)
- 96 C.J. Dasch, *Appl. Opt.* **23**, 2209 (1984)
- 97 G.J. Smallwood, D. Clavel, D. Gareau, R.A. Sawchuk, D.R. Snelling, P.O. Witze, B. Axelsson, W.D. Bachalo, Ö.L. Gülder, *SAE Tech. Paper Ser.* 2002-01-2715 (2002)
- 98 S.S. Krishnan, K.C. Lin, G.M. Faeth, *J. Heat Transf.* **122**, 517 (2000)
- 99 M.Y. Choi, G.W. Mulholland, A. Hamins, T. Kashiwagi, *Combust. Flame* **102**, 161 (1995)
- 100 M. Schnaiter, H. Horvath, O. Mohler, K.-H. Naumann, H. Saathoff, O.W. Schock, *J. Aerosol Sci.* **34**, 1421 (2003)
- 101 C.W. Bruce, T.F. Stromberg, K.P. Gurton, J.B. Mozer, *Appl. Opt.* **30**, 1537 (1991)
- 102 R.A. Dobbins, G.W. Mulholland, N.P. Bryner, *Atmos. Environ.* **28**, 889 (1994)
- 103 D.R. Snelling, K.A. Thomson, G.J. Smallwood, Ö.L. Gülder, E.J. Weckman, R.A. Fraser, *AIAA J.* **40**, 1789 (2002)
- 104 V. Beyer, D.A. Greenhalgh, *Appl. Phys. B* (2006), DOI: 10.1007/s00340-006-2238-6
- 105 H.A. Michelsen, *Appl. Phys. B* (2006), DOI: 10.1007/s00340-006-2226-x
- 106 K.A. Thomson, D.R. Snelling, G.J. Smallwood, F. Liu, *Appl. Phys. B* (2006), DOI: 10.1007/s00340-006-2198-x
- 107 J. Delhay, Y. Bouvier, E. Therssen, J.D. Black, P. Desgroux, *Appl. Phys. B* **81**, 181 (2005)
- 108 F. Cignoli, S. Benecchi, G. Zizak, *Appl. Opt.* **33**, 5778 (1994)
- 109 H. Geitlinger, T. Streibel, R. Suntz, H. Bockhorn, *Proc. Combust. Inst.* **27**, 1613 (1998)
- 110 S. Will, S. Schraml, A. Leipertz, *Proc. Combust. Inst.* **26**, 2277 (1996)
- 111 T.P. Jenkins, R.K. Hanson, *Combust. Flame* **126**, 1669 (2001)
- 112 F. Liu, M. Yang, F.A. Hill, D.R. Snelling, G.J. Smallwood, *Appl. Phys. B* (2006), DOI: 10.1007/s00340-006-2196-z
- 113 A. Eremin, E. Gurentsov, M. Hofmann, B. Kock, C. Schulz, *Appl. Phys. B* (2006), DOI: 10.1007/s00340-006-2199-9
- 114 M.Y. Choi, K.A. Jensen, *Combust. Flame* **112**, 485 (1998)
- 115 K.P. Geigle, Y. Schneider-Kühnle, M. Tsurikov, R. Hadeff, R. Lück-erath, V. Krüger, W. Stricker, M. Aigner, *Proc. Combust. Inst.* **30**, 1645 (2005)
- 116 A.V. Filippov, M. Zurita, D.E. Rosner, *J. Colloid Interf. Sci.* **229**, 261 (2000)
- 117 A.V. Filippov, D.E. Rosner, *J. Aerosol Sci.* **30**, S473 (1999)
- 118 D.R. Snelling, G.J. Smallwood, I.G. Campbell, J.E. Medlock, Ö.L. Gülder, Development and application of laser induced incandescence (LII) as a diagnostic for soot particulate measurements. In *AGARD 90th Symp. Propulsion and Energetics Panel on Advanced Non-Intrusive Instrumentation for Propulsion Engines*, Brussels, Belgium, 1997, 23.1
- 119 J. Hult, A. Omrane, A. Nygren, C.F. Kaminsky, B. Axelsson, R. Collin, P.-E. Bengtsson, M. Aldén, *Exp. Fluids* **33**, 265 (2002)
- 120 M. Charwath, R. Suntz, H. Bockhorn, *Appl. Phys. B* (2006), DOI: 10.1007/s00340-006-2265-3
- 121 B. Bougie, L.C. Ganippa, A.P. van Vliet, W.L. Mee rts, N.J. Dam, J.J. ter Meulen, *Combust. Flame*, in press (2006), DOI: 10.1016/j.combustflame.2006.03.002
- 122 B. Bougie, L.C. Ganippa, N.J. Dam, J.J. ter Meulen, *Appl. Phys. B* (2006), DOI: 10.1007/s00340-006-2195-0
- 123 S. Dankers, A. Leipertz, *Appl. Opt.* **43**, 3726 (2004)
- 124 S.-A. Kuhlmann, J. Schumacher, J. Reimann, S. Will, in *Int. Congr. Particle Technology (PARTEC 2004)*, Nürnberg, Germany (2004), paper No. 93
- 125 T. Lehre, Entwicklung einer berührungslosen in-situ Messmethode zur Bestimmung von Größenverteilungen nanoskaliger Teilchen, University of Karlsruhe (2005)
- 126 H. Bockhorn, F. Fetting, A. Heddrich, G. Wannemacher, *Ber. Bunsenges. Phys. Chem.* **91**, 819 (1987)
- 127 J. Lahaye, G. Prado, in *Particulate Carbon, Formation During Combustion*, ed. by D.C. Siegla, G.W. Smith (Plenum, New York, 1981), p. 33
- 128 A.R. Jones, *Prog. Energ. Combust. Sci.* **25**, 1 (1999)
- 129 C.M. Sorensen, *Aerosol Sci. Technol.* **35**, 648 (2001)
- 130 A. Doicu, T. Wriedt, *Opt. Commun.* **190**, 13 (2001)
- 131 P. Yang, K.N. Liou, M.I. Mishchenko, B.-C. Gao, *Appl. Opt.* **39**, 3727 (2000)
- 132 B.T. Draine, P.J. Flatau, *J. Opt. Soc. Am. A* **11**, 1491 (1994)
- 133 D.R. Snelling, K.A. Thomson, G.J. Smallwood, Ö.L. Gülder, *Appl. Opt.* **38**, 2478 (1999)
- 134 R.J. Santoro, H.G. Semerjian, R.A. Dobbins, *Combust. Flame* **51**, 203 (1983)
- 135 Ü.Ö. Köylü, C.S. McEnally, D.E. Rosner, L.D. Pfefferle, *Combust. Flame* **110**, 494 (1997)
- 136 C.S. McEnally, Ü.Ö. Köylü, L.D. Pfefferle, D.E. Rosner, *Combust. Flame* **109**, 701 (1997)
- 137 R.A. Dobbins, C.M. Megaridis, *Langmuir* **3**, 254 (1987)
- 138 R.L. Vander Wal, T.M. Tichich, A.B. Stephens, *Combust. Flame* **116**, 291 (1999)
- 139 R. Puri, T.F. Richardson, R.J. Santoro, R.A. Dobbins, *Combust. Flame* **92**, 320 (1993)
- 140 R.J. Santoro, J.H. Miller, *Langmuir* **3**, 244 (1987)
- 141 R.A. Dobbins, R.A. Fletcher, H.-C. Chang, *Combust. Flame* **115**, 285 (1998)
- 142 B.J. Stagg, T.T. Charalampopoulos, *Combust. Flame* **94**, 381 (1993)